

#### **DDC AVAILABILITY**

**Qualified requestors may obtain copies of this  
report from the Defense Documentation Center,  
Alexandria, Virginia 22314**

604192

tech ops

# TECHNICAL OPERATIONS RESEARCH

## DOSE RATE DISTRIBUTION IN A COMPARTMENTED STRUCTURE

By

M. J. Barrett  
R. L. MacNeil

COPY <u>2</u> OF <u>3</u>	
HARD COPY	\$ . 3.00
MICROFICHE	\$ . 0.75

Report No. TO-B 64-1

June, 1964

66p

### OCD REVIEW NOTICE

This report has been reviewed in the Office of Civil Defense and approved for publication. Approval does not signify that the contents necessarily reflect the views and policies of the Office of Civil Defense.

Prepared for

Office of Civil Defense  
Department of the Army-OSA  
Under  
Contract No. OCD-OS-62-14  
Subtask 1111A

**Burlington, Massachusetts**

## ACKNOWLEDGMENTS

The authors wish to thank Mr. William Barch, Mr. Sheldon Hunt, and Mr. James L. Jones for their assistance in the careful performance of the experiments; Miss Barbara Schacht for her patient handling of the multitude of calculations required; and Miss Barbara Copeland for her accurate preparation of the manuscript. Finally, we acknowledge the help of Dr. Eric T. Clarke for stimulating discussions of some of the problems encountered in the work.

# ABSTRACT

Measurements are reported of the gamma radiation-induced dose in a compartmented steel structure. The experimental dose profile is compared with predictions based on computational techniques in the Office of Civil Defense Engineering Guide, as well as with computations performed by the Monte Carlo technique. Although agreement (within experimental accuracy) is reached between the Monte Carlo and the experimental measurements, the OCD predictions appear to overestimate the dose because of an incomplete consideration of the effect of spacing of the structure slabs. The degree of conservatism does not appear to be serious, however.

# TABLE OF CONTENTS

<u>Chapter</u>		<u>Page</u>
1	INTRODUCTION . . . . .	1
2	DESCRIPTION OF EXPERIMENT . . . . .	3
	SITE . . . . .	3
	SOURCE . . . . .	3
	COLLIMATORS . . . . .	5
	SIMULATED BUILDING STRUCTURE (EGG CRATE) . . . . .	7
	INSTRUMENTATION . . . . .	8
	EXPERIMENTAL PROCEDURE . . . . .	9
	EXPERIMENTAL RUN AND DATA REDUCTION . . . . .	12
3	EXPERIMENTAL DATA . . . . .	16
4	ANALYSIS OF DATA . . . . .	24
	ATTENUATION BY FINITE SLABS OF NORMALLY INCIDENT RADIATION . . . . .	24
	ATTENUATION BY FINITE SLABS OF ISOTROPIC RADIATION . . . . .	26
	CONSTRUCTION OF ISOTROPIC SOURCE RESPONSE FROM MEASUREMENTS OF PARALLEL BEAM RESPONSE . . . . .	27
	COMPARISON WITH ROOFTOP CONTAMINATION CALCULATIONS . . . . .	32
5	COMPARISON WITH MONTE CARLO CALCULATIONS . . . . .	36
	RESULTS OF NORMAL INCIDENCE COMPUTATIONS . . . . .	37
	RESULTS OF SLANT INCIDENCE COMPUTATIONS . . . . .	41
	ISOTROPICALLY INCIDENT RADIATION . . . . .	42
6	CONCLUSIONS AND RECOMMENDATIONS . . . . .	46
	CONCLUSIONS . . . . .	46

## TABLE OF CONTENTS (Cont'd.)

<u>Chapter</u>		<u>Page</u>
6	SHIELDING .....	46
	METHODS OF SOLUTION .....	46
	RECOMMENDATIONS .....	47
	REFERENCES .....	48

## LIST OF ILLUSTRATIONS

<u>Figure</u>		
1	Gamma Ray Projector Housing Cobalt-60 Source Used in Experiments .....	4
2	Projector Housed in Lead Collimator .....	5
3	Schematic Diagram of Collimator System .....	6
4	Side Plate Being Installed on Instrumented Structure .....	8
5	Cross Configuration, with Relative Intensities of Gamma Radiation Incident on Structure .....	10
6	Compartmented Structure in Beam with Pivot Axis to Simulate Various Angles of Incidence .....	11
7	Compass Rose Constructed on Floor to Facilitate Positioning for Angular-Incidence Runs .....	13
8	Positioning of Rate Chamber for Experiments 17 and 18 .....	15
9	Detector Plane Showing Letter Code .....	16
10	Detector Planes in Structure .....	17
11	Horizontal Traverse of Radiation Field in Midplane of Each Compartment (Experiments 12 and 13) .....	23
12	Allowed Angles of $\Theta$ for Straight-Line Propagation of Radiation .....	27

## LIST OF ILLUSTRATIONS (Cont'd.)

<u>Figure</u>		<u>Page</u>
13	Construction for Determination of Eq. 3 . . . . .	28
14	Fraction of the Azimuthal Angle Range That Contributes Direct-Beam Radiation to a Detector in the Center of a Given Compartment . . . . .	29
15	Scattered Component of Dose Rates Along Centerline of Compartments, Due to Incident Radiation and Angles $\Theta$ with Normal to Front Plate . . . . .	31
16	Monte Carlo Program Simulation of Slab Shield Effects . . . . .	36
17	Comparison of Monte Carlo Prediction of Scattered Dose Rates with Centerline Measurements (Front compartment) . . . . .	38
18	Comparison of Scattered Component of Flux Due to Rooftop Radiation as Determined by Three Methods; Detector in Front Compartment of 40 psf Structure . . . . .	44
19	Monte Carlo and Transport Solutions for Scattered Flux; Detec- tor on Centerline of Front Compartment of 20 psf Structure . . .	44
20	Experimental Points and Transport Curve for Scattered Flux; Detector on Centerline of Center Compartment of 40 psf Structure . . . . .	45
21	Experimental Points and Transport Curve for Scattered Flux; Detector on Centerline of Rear Compartment of 40 psf Structure . . . . .	45

## LIST OF TABLES

<u>Table</u>		
1	Construction of Compartmented Structure for Each Experimental Run . . . . .	12
2	Experiment 1: Attenuation by 20 psf Walls, Without Top, Sides, and Bottom . . . . .	17
3	Experiment 2: Attenuation by 40 psf Walls, Without Top, Sides, and Bottom . . . . .	18

# LIST OF TABLES (Cont'd.)

<u>Table</u>		<u>Page</u>
4	Experiment 3: Attenuation by 80 psf Walls, Without Top, Sides, and Bottom . . . . .	18
5	Experiment 4: Attenuation by 40 psf Walls, With 40 psf Bottom . . . . .	19
6	Experiment 5: Attenuation by 40 psf Walls, With 40 psf Top and Bottom . . . . .	19
7	Experiment 6: Attenuation by 40 psf Complete Structure, With 40 psf Top, Bottom, Sides, and Walls . . . . .	20
8	Experiment 7: Attenuation by 40 psf Complete Structure, With Beam Incident at 15° from Normal . . . . .	20
9	Experiment 8: Attenuation by 40 psf Complete Structure, With Beam Incident at 30° from Normal . . . . .	21
10	Experiment 9: Attenuation by 40 psf Complete Structure, With Beam Incident at 45° from Normal . . . . .	21
11	Experiment 10: Attenuation by 40 psf Complete Structure, With Beam Incident at 60° from Normal . . . . .	22
12	Experiment 11: Attenuation by 40 psf Complete Structure, With Beam Incident at 75° from Normal . . . . .	22
13	Comparison of Narrow-Beam, Wide-Beam, and Finite-Beam Attenuation by Iron . . . . .	25
14	Components of Isotropic Roof Source Dose Contribution . . . . .	32
15	Comparison of Experimentally Derived and Theoretical Rooftop Source Dose Rates . . . . .	34
16	Comparison of Monte Carlo and Experimentally Derived Dose Rates for Normally Incident Beam on 20 psf Walls . . . . .	40
17	Comparison of Monte Carlo and Experimentally Derived Dose Rates for Slant Radiation on 40 psf Structure . . . . .	42



## CHAPTER 1

### INTRODUCTION

The study of radiation shielding has generated a large body of literature on the effects of matter in bulk on a gamma radiation field. These effects are normally found, both by theory and experiment, to be a reduction of the dose rate\* behind the matter and an increase of the dose rate in front of the matter, i. e., on the side adjacent to the gamma sources. The extent of the effect becomes less predictable for the cases of the matter forming a complicated structure such as one surrounding the field point, and here one resorts either to an artful combination of duct theories, albedo theories, and ray theories, or to the mathematical game of Monte Carlo played with a digital computer.

Such a problem—that of predicting the gamma radiation field within a shield of complicated structure—has a practical application. Should there ever be a nuclear attack on the United States, radioactive debris from nuclear weapons exploded on targets can be expected to shower down over large areas otherwise untouched by the effects of the explosions. In an idealized theoretical sense, this fallout can be expected to form a horizontal source plane over the ground, perhaps interrupted by patches suspended by building roofs and vegetation. These roofs, and the floors beneath, may provide a measure of protection to building occupants. Knowledge of the field reduction within the building is then of vital importance in the evaluation of fallout shelters.

Guides for the theoretical computation of such a field reduction have been published by the Office of Civil Defense.<sup>1,2</sup> These are based on empirical extrapolation of bulk shield studies of the radiation transport phenomena and are designed to include such cases as that of the present discussion. The methods presented in these OCD guides are intended to provide a close estimate of the ratio of the dose rate in the building at any given point, to the dose rate that would be experienced

---

\* Throughout this report, the words "dose rate" refer to the rate of creation of ion pairs in a unit volume of air-equivalent medium by the gamma field. The unit of measurement for dose rate, in this sense, is the roentgen per hour.

in the absence of the building 3 ft above the same field of fallout. This ratio is referred to as the "reduction factor," and its inverse as the "protection factor." A significant effect in this calculation is that provided by the removal of the portion of the source plane within the perimeter of the building walls to a position on the building roof.

The purpose of the present study was to measure this effect experimentally on an extremely simplified compartmented model structure, so that complicating features would not obscure the effect. A two-way comparison of experiment with theory was possible, since, in addition to the techniques available in Refs. 1 and 2, a digital computer calculation, applying a recently developed program based on Monte Carlo techniques, was made of the gamma field for a central point in the configuration studied.

Our shield configuration, then, was a structure made of iron slabs and resembling an egg crate with three compartments. The slabs corresponded to the roof, floors, and walls of a simplified building; their thicknesses were varied to span the range of areal densities encountered in present-day buildings. A beam of radiation from a strong cobalt-60 source was projected onto a square cross section subtended by the "roof" of the structure. Data for various structures, positions in the structure, and angles of the beam were obtained by timed exposures of 200 mr and 10 mr ionization chambers; some of the more critical measurements were made with a highly sensitive rate chamber in a Wheatstone bridge circuit. A more complete description of the experiment is given in Chapter 2.

The data obtained in these experiments are collected in Chapter 3, with an explanation of the methods used in correcting for various experimental complications.

In Chapter 4, the experimental data are analyzed and their computational techniques compared with those used in the OCD Engineering Guide.<sup>2</sup> The analysis continues in Chapter 5 with a comparison of experimental and Monte Carlo-calculated results. Here we see enough agreement to justify our confidence in the results derived by the Monte Carlo technique. Finally, conclusions and recommendations gained from this study are summarized in Chapter 6.

## CHAPTER 2

### DESCRIPTION OF EXPERIMENT

#### SITE

In the spring of 1960, Technical Operations Research constructed a facility to conduct an experimental radiation shielding program for the Office of Civil Defense. The following year, a vinyl-coated nylon hemisphere supported by a differential air pressure was erected on the facility test pad to provide shelter for all-weather operations. (The present experiments were performed during winter months.) As the facility has been discussed in an earlier report,<sup>3</sup> it will not be further discussed here except for some details that are pertinent to the present series of experiments.

Normally, the air pressure in the hemisphere, which is maintained by air blowers, is 14.75 psi. The mean free path of cobalt-60 radiation (used in the present experiment) is 445 ft in air at standard atmospheric pressure. The increased pressure in our facility slightly reduces this to 443 ft. The dimensions of the model structure used in the present experiment are so much smaller than these values, however, that one could reasonably assume no attenuation by air without introducing significant error.

The test pad of the facility has a flat surface of asphalt. To minimize the interference of gamma scattering from this surface, the experiment was conducted in a plane approximately 4 ft above the pad. Further, the use of thick shielding under the source prevented it from radiating directly to the floor, thus making the effects of floor scattering negligible in this experiment.

#### SOURCE

An encapsulated source of cobalt-60 was used for all experiments conducted. This source was compared on December 7, 1959, with one calibrated at the National Bureau of Standards against standard sources and was found at that time to have a strength of 102 curies. Based on a cobalt half-life of 5.28 yr, calculation shows that on October 17, 1963, when these experiments were initiated, the source strength was reduced to 61.7 curies.

The source was housed in a Tech/Ops Model 528 Gamma Ray Projector (Figure 1), which is essentially a container with 12-in. lead walls and a curved duct through which the source travels. The source is pushed out of the duct by a remotely controlled cable attached to the source and operated by a crank at the control console. Mechanical switches are built into the device and connected to indicator lights on the panel, so that the position of the source may be ascertained at a glance.

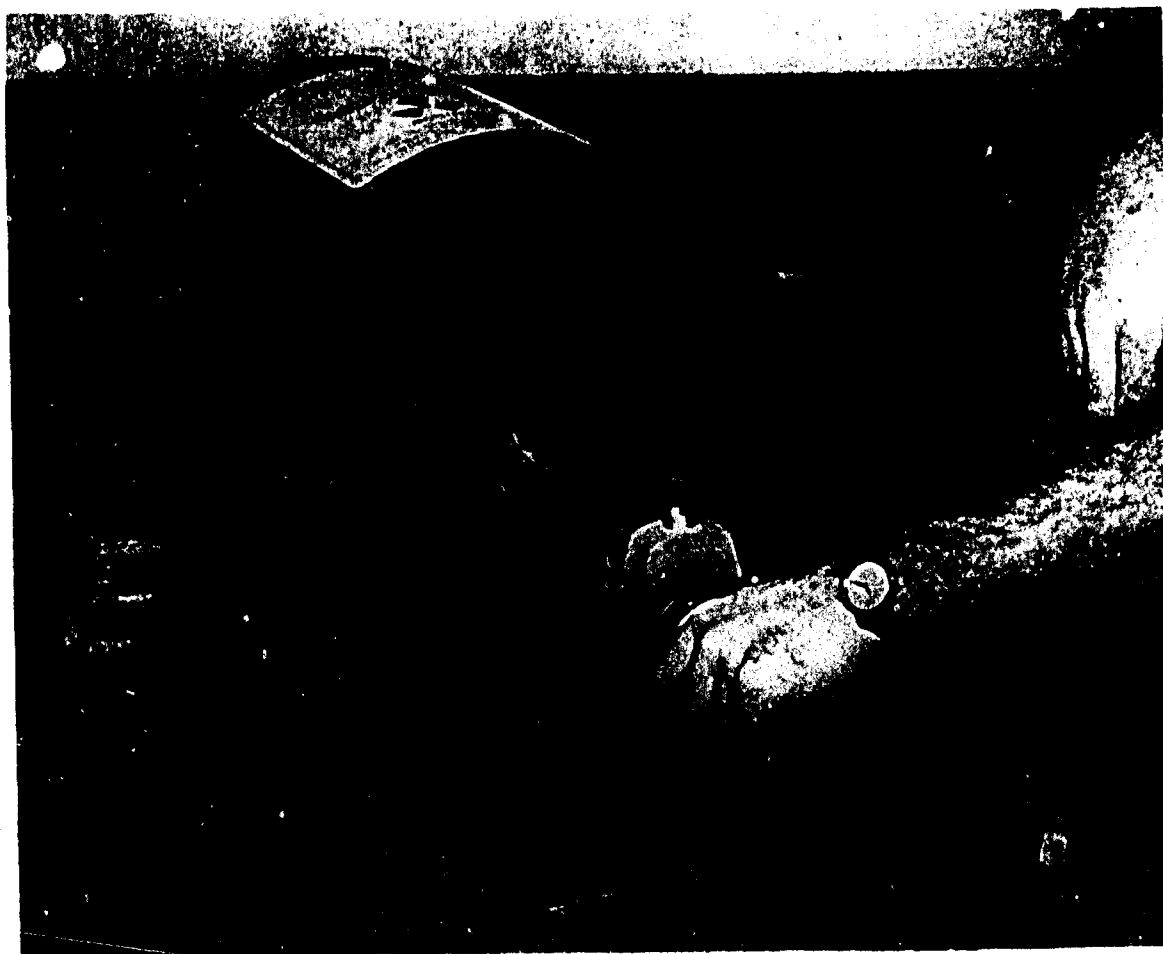


Figure 1. Gamma Ray Projector Housing Cobalt-60 Source Used in Experiments

The gamma ray projector was seated on a platform of concrete blocks. This platform also provided space for a lead collimator, which was placed directly in front of the projector aperture. A 1/2 in. steel plate on the platform made a firm surface for projector and collimator.

### COLLIMATORS

When the source was extended from the projector, it entered a lead chamber having a small opening that allowed a beam of nearly parallel radiation to be emitted. A lead slab with a square aperture through its center was the first collimator. This aperture tapered from an outer 2 in. square hole to an inner 1-5/8 in. square hole and collimated the beam so that it had a 2 ft square cross section at the experimental target. Figure 2 shows the source assembly with collimator and with a cylindrical disk of lead that may be rolled in front of the aperture. Figure 3 is a schematic diagram of the collimator apparatus. Lead and concrete shielding on all sides of the assembly reduced the surface dose rate to 2 mr/hr with source extended.

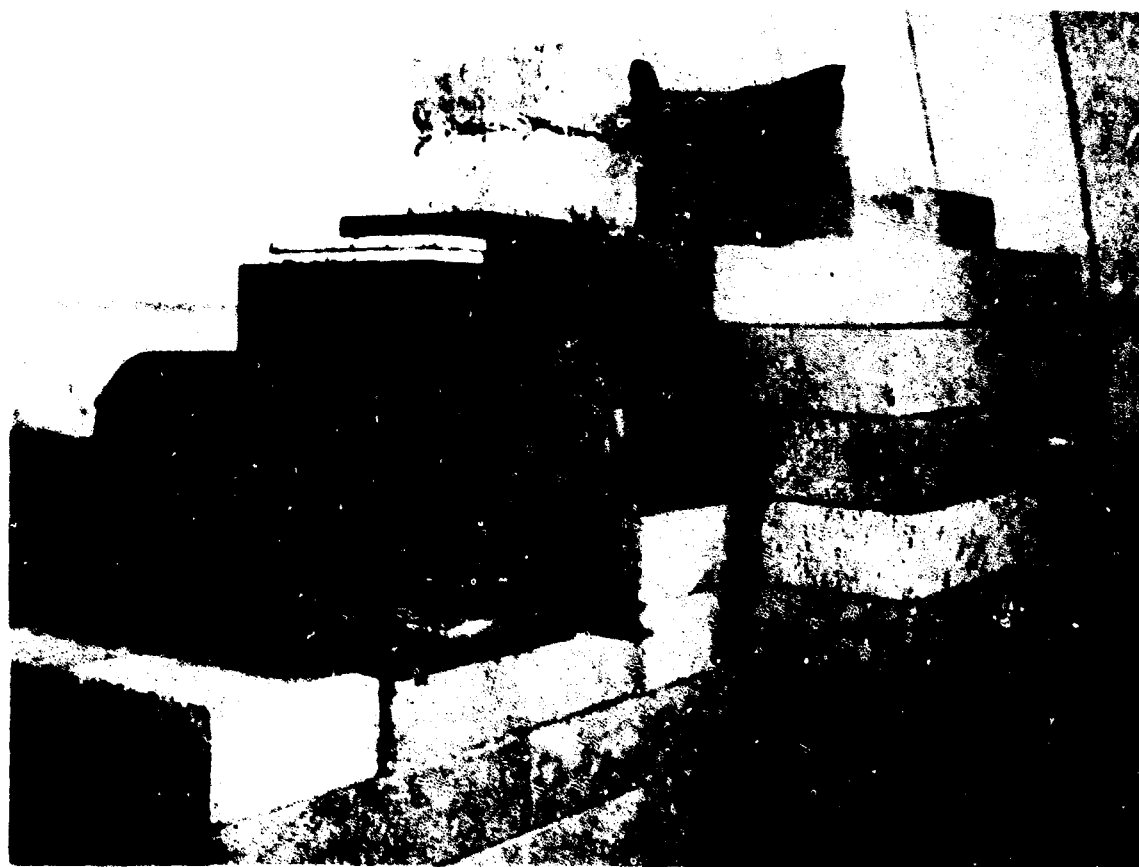


Figure 2. Projector Housed in Lead Collimator

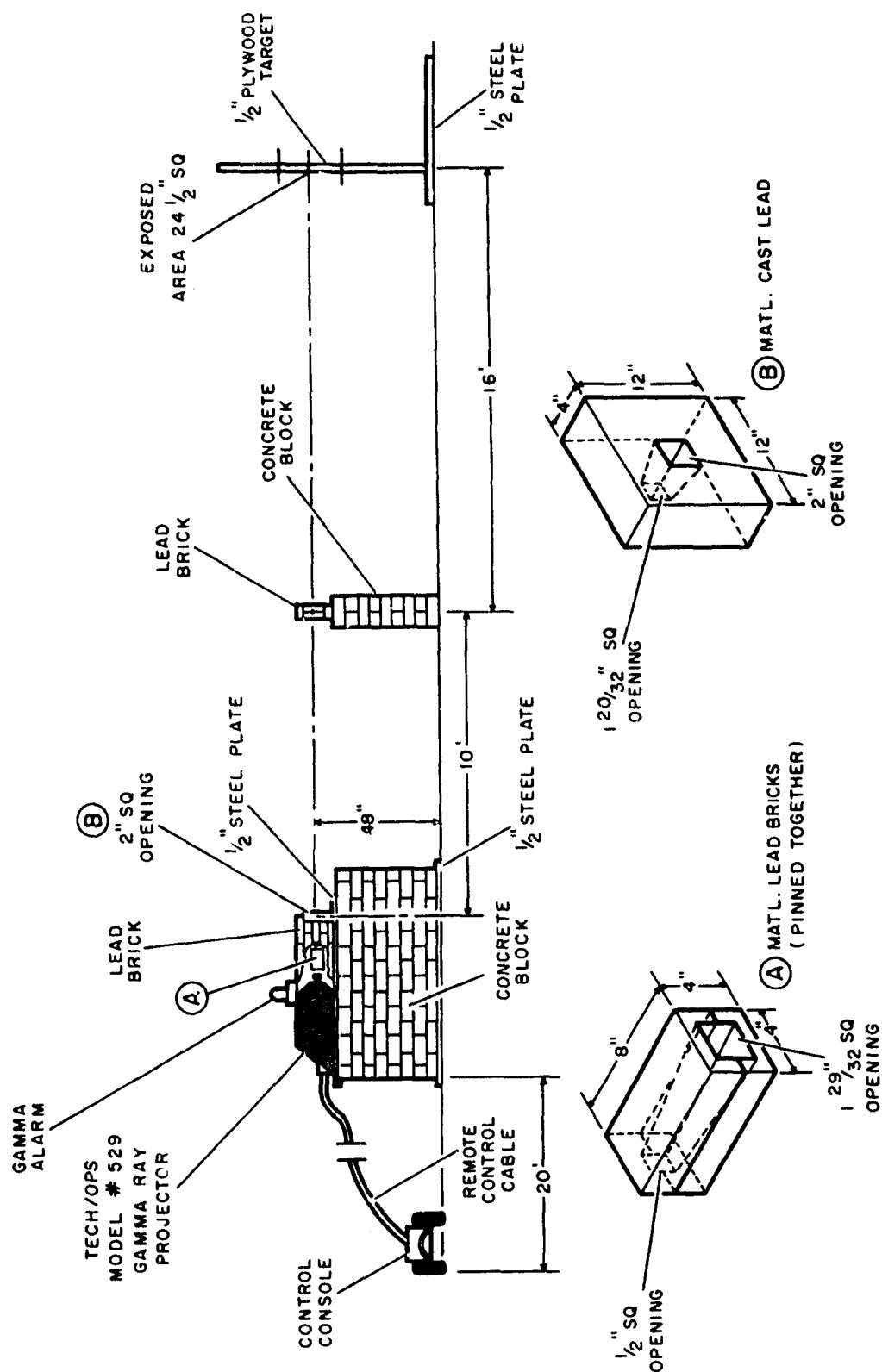


Figure 3. Schematic Diagram of Collimator System

A penumbral collimator was placed 10 ft from the first collimator. This collimator was constructed of 4 in. thick lead bricks, the top layer of which was supported by a steel plate, and stood on a concrete block pedestal. Since the beam widened with distance from the point source, the opening in this collimator was 12 in. square. The major purpose of this construction was to cut off those portions of the beam partially obstructed by the first collimator, thereby "shaping" a beam of almost constant intensity; some small angle air-scattering was probably also thus eliminated.

### SIMULATED BUILDING STRUCTURE (EGG CRATE)

The projector and collimator allowed a gamma beam of a square cross section with a maximum  $5^{\circ}$  spread to strike the experimental structure. During the course of the experiments, this structure was dubbed the "egg crate." The basic unit of the egg crate was four steel slabs, 1/2 in. thick and 2 ft square, each supported in a vertical plane by two steel legs, 2 in. x 1/2 in. x 36 in. The legs were connected by a cross strap and a base platform under the slabs, and the slabs positioned 1 ft apart. All these connections were made by spot-welding.

During the experiments, a bottom plate section was added to this basic unit. It was composed of three 1/2 in. thick plates, each of which fitted into the space between two adjacent slabs to form a floor. Side plates of the same thickness were later added, and these rested on tabs projecting from the legs. Finally, a top plate was laid over the basic unit to form a completely enclosed box with two internal partitions. All surfaces of the egg crate were painted with a thin coat of rust-resistant paint. Figure 4 shows a view of the instrumented egg crate just prior to installation of the final side plate.

The wall upon which the primary beam was incident, and all walls parallel to it, could be adjusted in thickness from 1/2 in. to 2.0 in., allowing a span of areal density range normal to building construction. Several measurements of the steel used gave an average weight of 41.2 psf of 1 in. steel plate.



Figure 4. Side Plate Being Installed on Instrumented Structure

#### INSTRUMENTATION

The majority of the dose measurements were made with uncompensated Victoreen Model 362 (200 mr) Pocket Chambers, positioned by insertion with their axes perpendicular to the primary beam in thin slabs (1/4 in.) of Styrofoam of a density of 0.033 g/cc. A preliminary experiment showed that the response of these chambers to incident ionizing radiation was essentially flat, provided that the chamber axis and the beam direction formed an angle greater than about  $15^{\circ}$ . (For smaller angles, the sensitivity dropped only about 15%.) The energy response of this instrument has been shown to be essentially air-equivalent down to photon energies of about 150 keV.<sup>4</sup> The decrease in charge of the chamber



(which is proportional to exposure) was measured with a Tech/Ops Model 556 Dosimeter Charger-Reader, a portable unit designed and constructed by this Company for field experiments.<sup>5</sup> The charge measurement was calibrated against chamber exposure in roentgens by use of a standard cobalt-60 source on a calibration range. Since response is a function of air density, corrections were made for temperature and pressure.

Where radiation levels were low, readings were made with Victorecn Model 239A Stray Radiation Chambers. These dosimeters, operating on the same principle as the 200 mr pocket chambers, fully discharge with an accuracy within 10% when exposed to 10 mr. They are essentially cylindrical—4.5 in. in length and 2.0 in. in diam. As a result, where radiation levels were low, total mapping of an area was not feasible because of the bulk of the detector.

A rate chamber was used for readings requiring extreme sensitivity but no precise positioning. The ionization rate chamber used has a volume of approximately 320 cc and is similar to the one found in a standard Victoreen Model 592 Survey Meter. The chamber signal, which is provided by ion currents across its electrodes and hence is proportional to the exposure rate, enters a low-noise, solid-state, feedback-type amplifier in the base of the chamber. The amplified output is smoothed through a simple RC circuit and fed to a John Fluke digital null voltmeter. Exposure rates as low as 0.01 mr/hr were thus read with excellent reproducibility. The rate chamber was required only for readings outside the egg crate. (Calibration of this instrument also requires corrections for air density, through the parameters of temperature and pressure.)

Personnel engaged in the experiments were equipped with 200 mr direct-reading dosimeters and film badges. The high radiation area was monitored continuously with a Tech/Ops Model 492 Gammalarm that provided a backup visual indication of the source position. During all manipulation of the structure or its instrumentation, two portable survey meters for personnel monitoring were used.

## EXPERIMENTAL PROCEDURE

Before any experimental data reported herein were taken, the cross-sectional outline of the collimated beam was determined.





Figure 6. Compartmented Structure in Beam with Pivot Axis to Simulate Various Angles of Incidence

## EXPERIMENTAL RUN AND DATA REDUCTION

Each run involved some difference in structure composition or orientation. Table 1 lists these briefly; they are described in more detail here.

TABLE 1  
CONSTRUCTION OF COMPARTMENTED STRUCTURE  
FOR EACH EXPERIMENTAL RUN

Exp. No.	Angle of Incidence (deg)	Front, Back, and Internal Wall Thickness (psf)	Side Wall Thickness (psf)			
			Top	Bottom	Left	Right
1	0	20	0	0	0	0
2	0	40	0	0	0	0
3	0	80	0	0	0	0
4	0	40	40	0	0	0
5	0	40	40	40	0	0
6	0	40	40	40	40	40
7	15	40	40	40	40	40
8	30	40	40	40	40	40
9	45	40	40	40	40	40
10	60	40	40	40	40	40
11	75	40	40	40	40	40
12	0	40	40	40	0	0
13	0	40	40	40	0	40
14	45	40	40	40	40	40
15	0	40	0	0	0	0
16	0	0	0	0	0	0

Experiments 1 through 3 were performed with no side, top, and bottom plates. Thus the configuration is that of four 2-ft square steel plates spaced 1 ft apart. The incident beam exactly covered the first plate. The thickness of the plates was 1/2 in. in the first three experiments, and it was doubled for each subsequent series of experiments.

Experiments 4 through 6, all performed with 1 in. plates, were a series designed to investigate the effects on the radiation field of adding plates that closed in the compartments. The top plate was added first, then the bottom, and then the sides.

Experiments 7 through 11 were performed on the fully completed structure and were designed to investigate the effects of slant incidence of the beam. Figure 7 shows the compass rose drawn on the floor for correct positioning of the structure, so that the projector beam would strike the front plate at the correct angle but would not strike the side plates.



Figure 7. Compass Rose Constructed on Floor to Facilitate Positioning for Angular-Incidence Runs

Experiments 12 and 13 were run to enable us to estimate the dose scattered into a compartment from the side walls with the beam at normal incidence to the structure. For this series of experiments we arrayed twenty-three chambers at 1 in. intervals so that they horizontally traversed the center of the front compartment. The chambers were positioned vertically. Experiment 12 was run without side plates, while Experiment 13 was run with one side plate installed. Thus, the difference in dose rates measured at each position for these two experiments can be attributed to scatter from the side plate.

Experiment 14 was run to check the accuracy with which we could place the structure for runs at other than normal incidence to the beam. The same array of chambers was used as in Experiments 12 and 13. The box structure was placed at  $45^{\circ}$  incident to the beam.

Experiment 15 was run to ascertain whether any detectable stray radiation at the outer fringe of the collimated beam could scatter into the front compartment upon striking high density material. Specifically, this would indicate if a correction would have to be made for scattering off the legs of the box-type structure. This experiment was essentially a repeat of Experiment 2, but a steel bar (with a 1 in. square cross section) was placed on top of the front plate. Any significant deviation between the results of this experiment and Experiment 2 would indicate that the beam overlapped the target, and scattering of the fringe radiation would be significant. Plotting the dose rates against the position of each chamber should result in a curve that breaks steeply at the edge of the direct beam. This would give a good indication of the accuracy of alignment of the box-type structure with the collimated beam.

Experiment 16 was a phantom structure experiment run primarily as a calibration. The box structure was removed, and in its place a light plywood panel was positioned to correspond with the front plate of the box. We then cut out of the panel a 2 sq ft opening aligned in the path of the collimated beam. Masking tape was used to install nine pocket chambers in this opening, at positions corresponding to those used during box experiments and at a depth corresponding to the front surface of the front plate of the box structure (at the normal angle of incidence).

Experiments 17 and 18 were a further attempt to read scatter back into the box from a side plate with the beam at a normal incidence. For this series, the ionization rate chamber was placed at points 1 through 5 as shown in Figure 8. Readings were taken with both sides removed from the box and also with alternate sides installed.

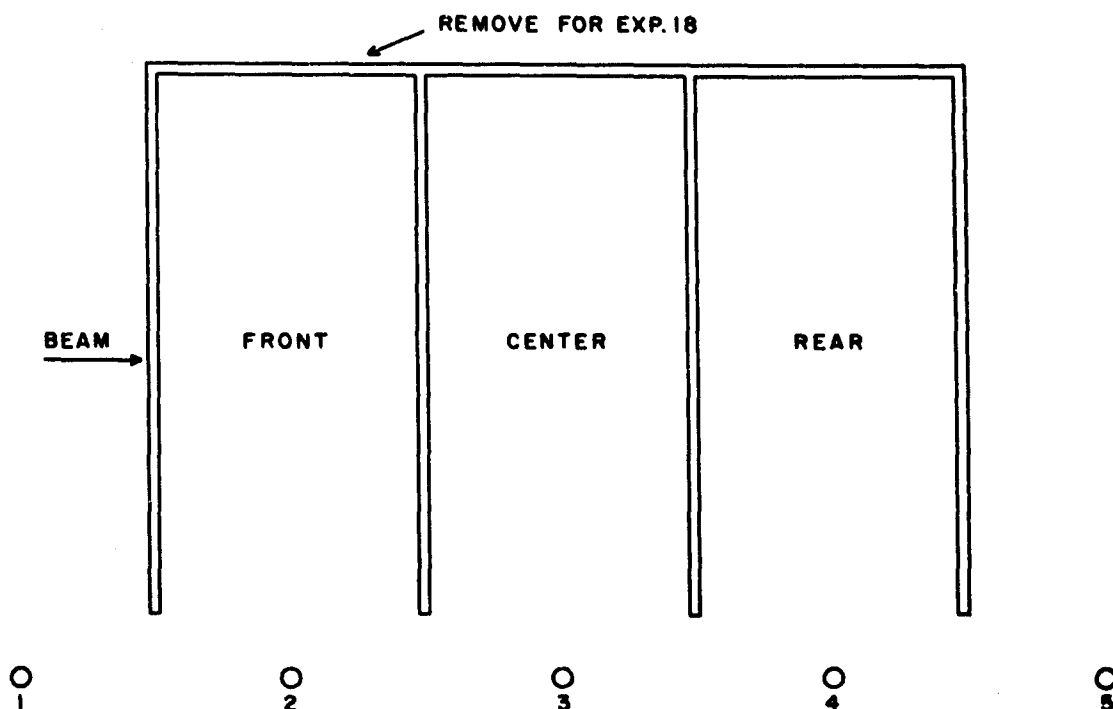


Figure 8. Positioning of Rate Chamber for Experiments 17 and 18

All data given in the tables are in terms of r/hr, assuming a 1 r/hr dose rate at the position with the structure removed. Thus, all data may be reduced to ratios of exposure rates of interest to the exposure rate in the incident beam. Chamber readings were converted to dose rates by multiplying by a constant that was determined by calibration against a standard source in air. The calibration constant, plus the temperature and pressure corrections postulated by air-wall ionization chamber theory, relate the chamber exposure to the readout measurement  $\mu a$  by the formula

$$D = \frac{T}{8.65P} \mu a ,$$

where T is in degrees Rankine, P in inches of mercury, and D in milliroentgens.

## CHAPTER 3

### EXPERIMENTAL DATA

Unless otherwise indicated, ion chambers were positioned in each of the three egg crate compartments in three vertical planes, with nine chambers to a plane. Thus this total of eighty-one readings per exposure provided excellent detail of the radiation field. The compartments are identified as front, center, and rear, with reference to the nearness to the radiation source; the instrument planes are similarly identified as 2, 6, and 10, representing their distances in inches from the front of the respective compartment. Detectors in each plane were spaced 8 in. apart; these are identified by the letter code shown in Figure 9. The planes are sketched in Figure 10. Note that detectors E, O, and Y are closest to the pivot axis used in Experiments 11 and 14.

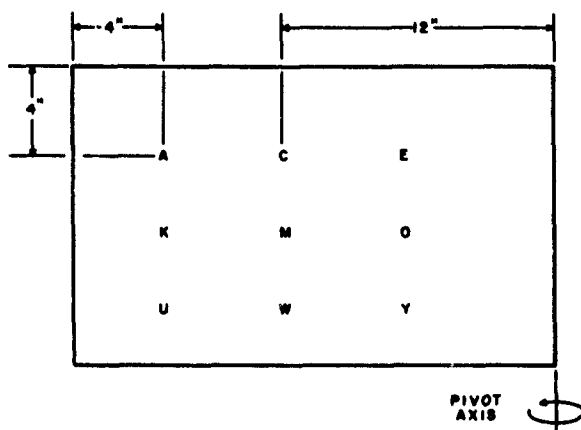


Figure 9. Detector Plane Showing Letter Code

Dividing measured chamber exposure by exposure time results in measured dose rates. These were corrected for temperature and pressure effects as mentioned above. The dose rates thus obtained were divided by dose rates measured at the location of the front slab of the structure (with the structure absent). This ratio is, of course, affected by the source-detector distance, and to correct for this, a factor of the ratio of the squares of the dis-

tances of the detector and the front plate was used. Finally, a 1.05 factor was used to correct for the presence of about 5% soft radiation (backscatter or X-rays from the projector), which was suggested by later single-slab measurements. With these corrections, the basic data are presumed to be normalized to a monoenergetic parallel-ray beam of radiation that has unit intensity as it strikes the structure being examined.

The basic data obtained in Experiments 1 through 11 and corrected as stated above are presented in Tables 2 through 12.



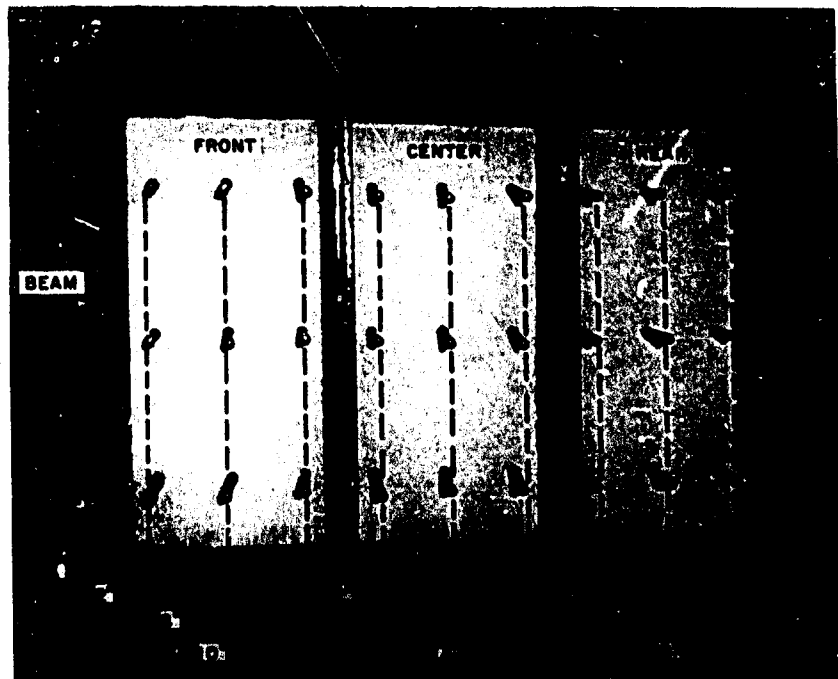


Figure 10. Detector Planes in Structure

TABLE 2

EXPERIMENT 1: ATTENUATION BY 20 PSF WALLS,  
WITHOUT TOP, SIDES, AND BOTTOM

Compartment	Detector Plane (in.)	Detector Position								
		A	C	E	K	M	O	U	W	V
Front	2	0.78	0.80	0.79	0.83	0.84	0.82	0.80	0.81	0.79
	6	.73	.74	.74	.77	.79	.77	.73	.74	.73
	10	.69	.70	.70	.70	.74	.70	.70	.70	.70
Center	2	.57	.59	.57	.57	.59	.59	.57	.55	.57
	6	.53	.55	.52	.54	.55	.53	.54	.54	.52
	10	.49	.50	.49	.50	.50	.48	.49	.50	.49
Rear	2	.54	.36	.34	.36	.41	.36	.34	.36	.34
	6	.31	.32	.32	.31	.37	.34	.30	.34	.31
	10	.29	.30	.29	.30	.34	.30	.29	.32	.29

TABLE 3  
EXPERIMENT 2: ATTENUATION BY 40 PSF WALLS,  
WITHOUT TOP, SIDES, AND BOTTOM

Compartment	Detector Plane (in.)	Detector Position								
		A	C	E	K	M	O	U	W	V
Front	2	0.55	0.56	0.54	0.59	0.59	0.59	0.58	0.58	0.60
	6	.50	.52	.49	.52	.54	.52	.49	.50	.50
	10	.45	.48	.45	.48	.51	.48	.46	.48	.46
Center	2	.24	.24	.24	.25	.25	.25	.24	.24	.23
	6	.21	.23	.21	.23	.24	.23	.21	.23	.19
	10	.19	.21	.19	.21	.22	.21	.19	.22	.18
Rear	2	.090	.097	.094	.100	.109	.097	.096	.094	.092
	6	.083	.093	.084	.088	.097	.089	.081	.089	.083
	10	.078	.087	.078	.082	.088	.082	.076	.084	.075

TABLE 4  
EXPERIMENT 3: ATTENUATION BY 80 PSF WALLS,  
WITHOUT TOP, SIDES, AND BOTTOM

Compartment	Detector Plane (in.)	Detector Position								
		A	C	E	K	M	O	U	W	V
Front	2	0.30	0.31	0.30	0.31	0.32	0.31	0.31	0.31	0.31
	6	.26	.28	.26	.28	.31	.30	.26	.27	.26
	10	.22	.27	.26	.26	.29	.26	.23	.26	.23
Center	2	.052	.057	.054	.057	.060	.056	.052	.054	.052
	6	.046	.052	.048	.049	.056	.050	.045	.050	.045
	10	.041	.047	.042	.044	.051	.046	.041	.046	.042
Rear	2	.0090	.0101	.0094	.0097	.0118	.0102	.0088	.0104	.0088
	6	.0080	.0088	.0080	.0087	.0102	.0089	.0079	.0094	.0076
	10	.0079	.0078	.0074	.0083	.0089	.0087	.0078	.0084	.0075

TABLE 5  
EXPERIMENT 4: ATTENUATION BY 40 PSF WALLS, WITH 40 PSF BOTTOM

Compartment	Detector Plane (in.)	Detector Position								
		A	C	E	K	M	O	U	W	V
Front	2	0.55	0.58	0.55	0.61	0.61	0.61	0.59	0.61	0.60
	6	.50	.52	.50	.53	.56	.53	.52	.54	.50
	10	.44	.49	.46	.50	.52	.48	.48	.50	.47
Center	2	.24	.24	.25	.25	.27	.25	.24	.25	.23
	6	.21	.21	.21	.21	.25	.23	.20	.24	.20
	10	.19	.21	.21	.21	.22	.21	.21	.22	.19
Rear	2	.099	.108	.099	.101	.116	.106	.098	.109	.102
	6	.085	.096	.085	.092	.103	.094	.081	.098	.094
	10	.083	.087	.079	.083	.093	.083	.075	.089	.083

TABLE 6  
EXPERIMENT 5: ATTENUATION BY 40 PSF WALLS, WITH 40 PSF TOP AND BOTTOM

Compartment	Detector Plane (in.)	Detector Position								
		A	C	E	K	M	O	U	W	V
Front	2	0.54	0.58	0.56	0.59	0.61	0.60	0.58	0.59	0.58
	6	.49	.52	.48	.52	.55	.53	.49	.52	.50
	10	.45	.49	.45	.48	.51	.48	.45	.49	.46
Center	2	.23	.25	.24	.24	.25	.24	.23	.23	.22
	6	.21	.23	.21	.20	.24	.21	.20	.21	.20
	10	.19	.22	.19	.19	.23	.21	.18	.21	.18
Rear	2	.096	.102	.094	.096	.107	.099	.094	.103	.096
	6	.079	.093	.083	.087	.094	.087	.079	.093	.087
	10	.080	.088	.076	.080	.087	.080	.072	.087	.076

TABLE 7

EXPERIMENT 6: ATTENUATION BY 40 PSF COMPLETE STRUCTURE, WITH  
40 PSF TOP, BOTTOM, SIDES, AND WALLS

Compartment	Detector Plane (in.)	Detector Position								
		A	C	E	K	M	O	U	W	V
Front	2	0.55	0.58	0.55	0.59	0.59	0.59	0.58	0.59	0.59
	6	.50	.53	.49	.53	.54	.55	.50	.53	.50
	10	.46	.49	.47	.49	.51	.48	.48	.49	.47
Center	2	.23	.25	.25	.25	.27	.25	.23	.23	.23
	6	.21	.24	.23	.21	.24	.23	.20	.21	.20
	10	.21	.22	.21	.21	.23	.21	.19	.21	.19
Rear	2	.098	.102	.098	.098	.112	.102	.096	.106	.098
	6	.087	.093	.087	.089	.098	.090	.080	.097	.089
	10	.080	.088	.078	.082	.091	.082	.074	.091	.078

TABLE 8

EXPERIMENT 7: ATTENUATION BY 40 PSF COMPLETE STRUCTURE,  
WITH BEAM INCIDENT AT 15° FROM NORMAL

Compartment	Detector Plane (in.)	Detector Position								
		A	C	E	K	M	O	U	W	V
Front	2	0.55	0.55	0.53	0.59	0.58	0.56	0.55	0.56	0.55
	6	.54	.53	.45	.57	.54	.47	.50	.50	.47
	10	.50	.50	.32	.52	.52	.35	.48	.48	.31
Center	2	.25	.25	.13	.27	.25	.14	.24	.23	.12
	6	.24	.23	.087	.24	.24	.094	.21	.21	.076
	10	.22	.22	.062	.22	.22	.062	.21	.19	.053
Rear	2	.098	.096	.023	.109	.106	.025	.099	.096	.021
	6	.089	.085	.021	.096	.090	.024	.085	.084	.021
	10	.084	.075	.018	.089	.082	.022	.079	.075	.018

TABLE 9

EXPERIMENT 8: ATTENUATION BY 40 PSF COMPLETE STRUCTURE,  
WITH BEAM INCIDENT AT 30° FROM NORMAL  
(See Figure 7)

Compartment	Detector Plane (in.)	Detector Position								
		A	C	E	K	M	O	U	W	V
Front	2	0.50	0.52	0.39	0.52	0.53	0.40	0.50	0.52	0.40
	6	.48	.47	.15	.46	.48	.19	.47	.46	.16
	10	.44	.44	.072	.48	.47	.078	.44	.42	.065
Center	2	.20	.19	.021	.21	.20	.024	.20	.17	.020
	6	.18	.114	.021	.19	.12	.025	.17	.106	.020
	10	.16	.055	.018	.17	.068	.023	.16	.052	.021
Rear	2	.069	.018	.0079	.079	.020	.0085	.070	.016	.0072
	6	.053	.014	.0078	.059	.018	.0088	.053	.014	.0074
	10	.034	.013	.0075	.038	.014	.0085	.034	.013	.0075

TABLE 10

EXPERIMENT 9: ATTENUATION BY 40 PSF COMPLETE STRUCTURE,  
WITH BEAM INCIDENT AT 45° FROM NORMAL

Compartment	Detector Plane (in.)	Detector Position								
		A	C	E	K	M	O	U	W	V
Front	2	0.39	0.42	0.32	0.42	0.42	0.33	0.39	0.40	0.33
	6	.38	.36	.069	.37	.38	.076	.36	.36	.060
	10	.35	.26	.045	.37	.26	.049	.35	.23	.040
Center	2	.061	—	—	.067	—	—	.064	—	—
	6	.049	.025	.013	.049	.027	.014	.046	.023	.0113
	10	.018	—	—	.021	—	—	.023	—	—
Rear	6	.0087	.0065	.0048	.0099	.0071	.0052	.0087	.0063	.0048

TABLE 11

EXPERIMENT 10: ATTENUATION BY  
40 PSF COMPLETE STRUCTURE, WITH  
BEAM INCIDENT AT 60° FROM NORMAL

Compartment	Detector Plane (in.)	Detector Position								
		A	C	E	K	M	O	U	W	V
Front	2	0.23	0.23	0.034	0.24	0.26	0.037	0.23	0.26	0.034
	6	.21	.084	.021	.21	.099	.024	.21	.084	.021
	10	.101	.042	.018	.12	.042	.021	.093	.042	.018
Center	6	.015	.0106	.0106	.018	.013	.0111	.014	.0102	.0102
Rear	6	.0034	.0024	.0027	.0037	.0030	.0030	.0032	.0024	.0026

TABLE 12

EXPERIMENT 11: ATTENUATION BY  
40 PSF COMPLETE STRUCTURE, WITH  
BEAM INCIDENT AT 75° FROM NORMAL

Compartment	Detector Plane (in.)	Detector Position								
		A	C	E	K	M	O	U	W	V
Front	2	0.063	—	—	0.069	—	—	0.064	—	—
	6	.034	0.021	0.0058	.036	0.023	0.0067	.033	0.019	0.0055
	10	.020	—	—	—	—	—	.020	—	—
Center	6	.0038	.0055	.0039	.0043	.0061	.0052	.0036	.0052	.0046
Rear	6	.00097	.0014	.0014	.0107	.0014	.0014	.00101	.0014	.0014

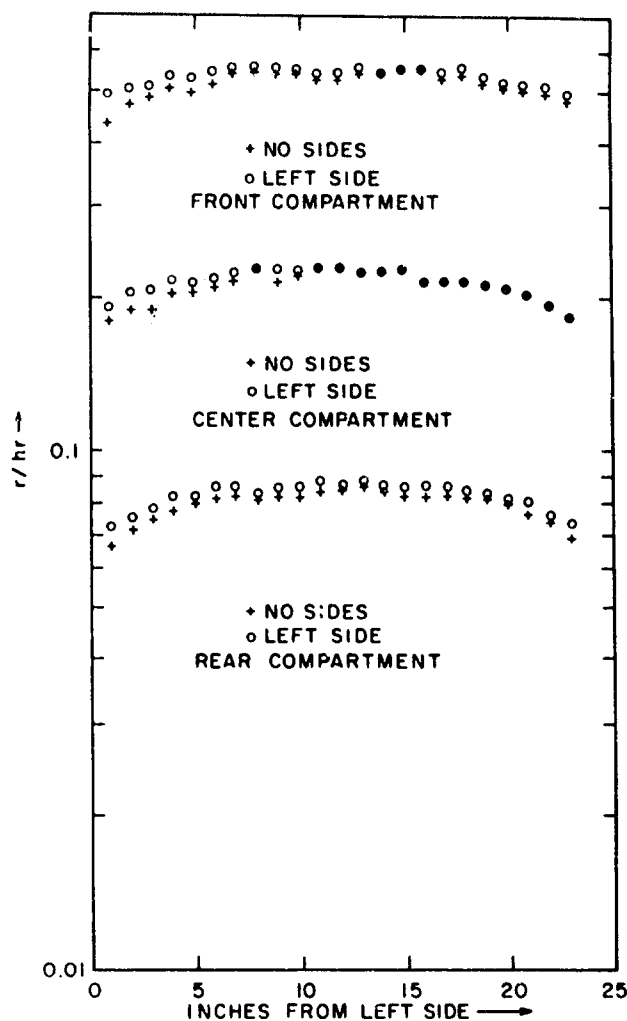


Figure 11. Horizontal Traverse of Radiation Field in Midplane of Each Compartment (Experiments 12 and 13)

Results of Experiments 12 and 13, designed for a more detailed investigation of the field profile in the structure normal to the beam, are graphed in Figure 11. Since the chambers were only 1 in. apart, it was possible to see the edge effects as the side of the structure was approached. Incidentally, this figure provides a demonstration of the accuracy of the instrumentation in that no points deviate more than about 4% or 5% of their positions on a smooth curve joining their neighbors.

Experiments 14 and 15—essentially checks on the accuracy of positioning of the structure—gave negative results; that is, no detectable differences existed in these configurations from dose rates received in similar experiments run previously. (Fundamentally, Experiments 14 and 15 were repeats of Experiments 12 and 2 respectively.

Finally, Experiment 16 showed that the front of the structure received a dose rate of 1.09 r/hr. This figure was used to determine the ratios reported in Tables 2 through 12.

## CHAPTER 4

### ANALYSIS OF DATA

#### ATTENUATION BY FINITE SLABS OF NORMALLY INCIDENT RADIATION

The gamma energy flux resulting from photons that have undergone no interaction since their birth and impinging on a small isotropic detector is given by the integral over all space of the source density (energy/sec/cc) at a distance  $r$ , divided by the quantity

$$4\pi r^2 \exp \int_0^r \mu(r) dr, \quad (1)$$

where  $\mu(r)$  is the linear attenuation coefficient of the medium at the point being traversed by the photon. The attenuation coefficient depends on the photon energy and the density and nature of the substances being traversed.

Rarely does this calculated value of the energy flux due to uncollided photons approach the true flux at the detector. Scattered radiation usually increases the response of the detector by a factor  $B$ , referred to as the "buildup factor" for the effect in question. Exact values of  $B$ , which are generally for simple geometries such as point sources in infinite media, are obtained with difficulty only by arduous machine calculations.

As an example, consider that the centerline detector responses in the egg crate have normal-beam incidence. This apparently simple geometry—four square slabs with a beam of parallel radiation striking the outer surface of the first—provides experimental values of  $B$  that are to be analyzed in the light of previous calculations.

Placing a detector in the center of the first compartment, we get a response (Table 3) that is 0.54 of that obtained with the egg crate removed. The 1 in. slab provides 1.07 mfp to the ray; this results in a narrow beam attenuation factor of



0.343. Thus, the value of B is 1.525; the additional 52.5% must be attributed to radiation that either

- (1) penetrates the slab as scattered radiation, or
- (2) rebounds from the posterior slabs as an albedo effect.

The energy albedo of iron for cobalt radiation is about 0.025.<sup>6</sup> The albedo depends, of course, on the angular distribution of the incident radiation and on the thickness of the iron, but the precise size of the effect is obviously of little importance and may be taken into account here by accepting this figure as the albedo  $\alpha$ . Most of the observed buildup is therefore due to process (1).

Spencer<sup>7</sup> has reported a number of calculations of the attenuation of cobalt radiation through concrete. He defines a function  $s(X, \Theta_0)$  that gives the dose attenuation by concrete of X psf thickness for radiation from a source plane infinite in extent, with all radiation leaving the plane at an angle  $\Theta_0$  to the normal. Now  $s(X, \Theta_0)$  readily provides us with an upper limit to the detector response, to be achieved only when the iron slabs are infinite planes, while the exponential function provides us with a lower limit that is approached only as the lateral extent of slabs and detector vanishes to zero. Table 13 gives these limits, together with centerline detector responses, and shows that, indeed, the pragmatic case of finite slabs does fall between the limits.

TABLE 13  
COMPARISON OF NARROW-BEAM, WIDE-BEAM, AND  
FINITE-BEAM ATTENUATION BY IRON

$\mu t$	Narrow-Beam $e^{-\mu t}$	Wide-Beam $s(X)$	Measured $D(X)$
1.07	0.343	0.690	0.54
2.14	.118	.385	.24
3.21	.040	.160	.097

Since the spread in predictions is much too wide, an expression for the buildup that incorporates a correction for the effect of slab extent is required.

One method for handling this problem is the Monte Carlo calculation<sup>8</sup> to be discussed in Chapter 5. The results compare fairly closely with the experimental values. For a slab thickness of 1.07 mfp, the result calculated by the Monte Carlo method is 0.558—a difference from experimental values of less than 2%.

## ATTENUATION BY FINITE SLABS OF ISOTROPIC RADIATION

From the results given for the parallel-beam case above, we expect similar behavior trends for the case where the incident radiation is isotropic. The trends are more complex, since now various angles of incidence are involved. One would expect that the extent of the slab would still affect the measured dose rate, however, and that a construction of the buildup function from angular and depth components would be possible. The Engineering Manual<sup>2</sup> presents theoretical comparisons for the results of such a construction. The curves presented therein for the evaluation of rooftop contamination are formed by the product  $L(X)L_c(X, \omega)$  obtained by Spencer. In such a case,  $L(X)$  is the attenuation of the isotropic infinite-layer source by material of thickness  $X$  and corresponds to a more precise evaluation of the dose rate (this is for an infinite slab and an isotropic source!), while  $L_c(X, \omega)$  is the fraction of the radiation at  $X$  resulting from the part of the plane source that subtends the solid angle fraction  $\omega$  at the detector.

The methods presented do not, however, make provision for the air spaces between detector and slab and for the division of the slab into layers. Therefore, it is of interest to compare results obtained experimentally with results obtained from curves of  $LL_c$ . Although this cannot be done for the parallel-beam situation, it can be done for the isotropic beam.

To simulate an isotropic beam, we directed the parallel beam at the egg crate at the different angles with the normal, as discussed in Chapter 2. It was then possible to perform a summation, suitably weighted over the angles of incidence, of the dosimeter exposures obtained and to compare this with predictions for

isotropic emission from the face of the first slab. Because this summation had to be done with care, the method described below was derived for a correct weighting and summing of the exposures.

### CONSTRUCTION OF ISOTROPIC SOURCE RESPONSE FROM MEASUREMENTS OF PARALLEL BEAM RESPONSE

For each angle  $\Theta$  that the rays make with the normal to the slabs, there is a range of azimuthal angles  $\phi$  that contributes no direct beam to a given detector. For a simple example of this forbidden range, consider a detector in the center of the middle compartment. From Figure 12, it can be seen that rays with angles  $\Theta$  less than or equal to  $\Theta_1$  strike the detector with all angles  $\phi$ , but rays with angles greater than this are restricted to four ranges of  $\phi$  that correspond to the corners of the top plate. Finally, no rays of angles  $\Theta$  equal to or greater than  $\Theta_2$  may strike this detector without having first scattered.

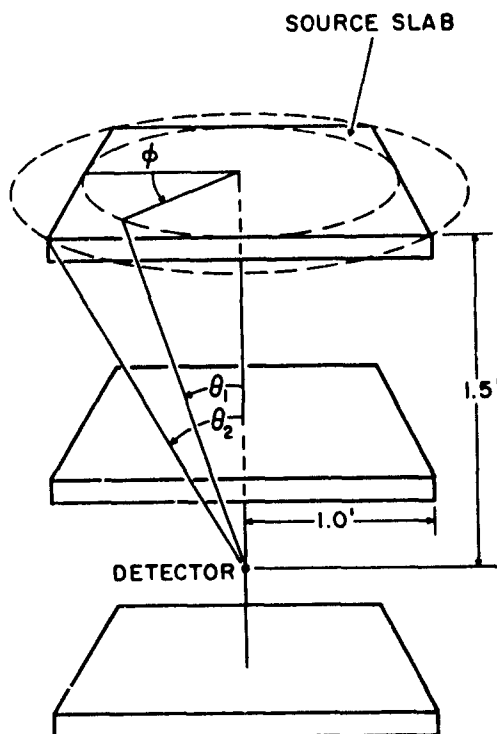


Figure 12. Allowed Angles of  $\Theta$  for Straight-Line Propagation of Radiation

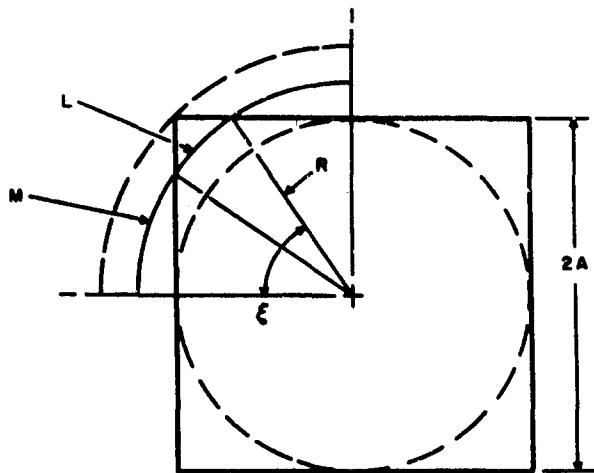


Figure 13. Construction for Determination of Eq. 3

The fraction of acceptable angles  $\phi$  to the total range of angles can be determined by geometric considerations for the cases between  $\Theta_1$  and  $\Theta_2$  for center-line detectors. Consider the circle of loci of sources positioned on the front plate to emit at angle  $\Theta$  (and, arbitrary,  $\phi$ ) so as to strike the detector with direct rays. The fraction sought is then the fraction of the circle that is on the plate. With the notation of Figure 13, this is equal to  $(4L)/(2\pi R)$ ; it can also be seen from the figure that

$$\sin \xi = \frac{A}{R}, \quad (2a)$$

$$(L + M) = \xi R, \quad (2b)$$

and

$$L + 2M = \frac{\pi}{2} R. \quad (2c)$$

With these identities, the range of  $\phi$  is given by

$$\frac{1}{2\pi} \int_0^{2\pi} p(\phi, \Theta) d\phi = \frac{4}{\pi} \arcsin \left( \frac{A}{Z} \cot \Theta \right) - 1, \quad (3)$$

where  $2A$  is the length of a side of the square plate, and  $Z$  is the distance of the detector from the plate. The range is plotted in Figure 14 for detectors in the centers of each of the three compartments.

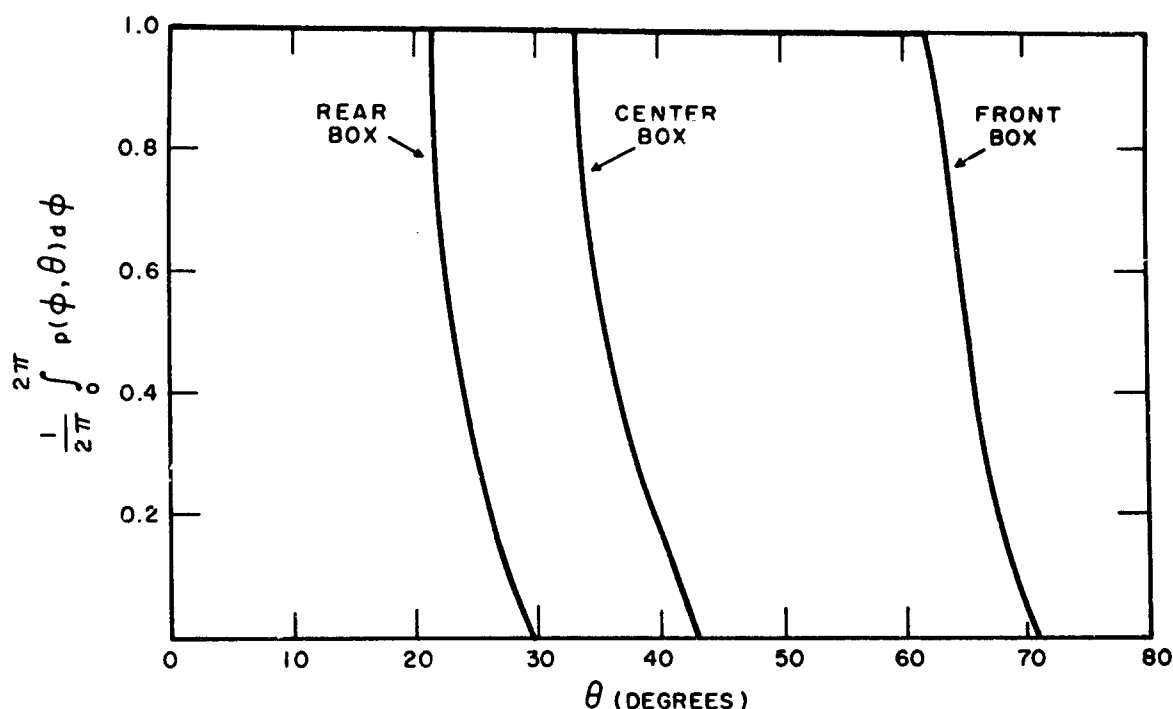


Figure 14. Fraction of the Azimuthal Angle Range That Contributes Direct-Beam Radiation to a Detector in the Center of a Given Compartment

As stated in the beginning of this chapter, the direct-beam component of the radiation is attenuated exponentially, while the scattered component behaves according to much more complex laws. Therefore, we assume our knowledge of the direct-beam component is correct; in particular, we subtract from the experimental data an analytic function corresponding to the direct beam. This function has a sharp cutoff, as discussed above. The residual component, however, can be expected to behave fairly smoothly, which allows us to integrate it numerically over all angles using a small number of intervals. (Because the detectors are not at ideal points, the cutoff is often not sharp enough; thus some angles provide measurements at some detectors that are not usable in this analysis.)

An analytic function describing the direct beam at a centerline detector due to radiation incident on the front plate with angle  $\Theta$  to the normal is  $\exp[-\lambda \sec \Theta]$ , where  $\lambda$  is the mean-free-path thickness of slabs in front of the detector. Integration

of this function over a source area gives the unscattered beam dose rate  $D_u$  for an isotropic rooftop source as

$$D_u = \int_A \frac{dA e^{-\lambda \sec \Theta}}{2\pi \rho^2} . \quad (4)$$

For a detector at a distance  $z$  from a square, with a shielded source area of size  $2a$ , the unscattered component is

$$D_u = \int_0^a \frac{e^{-\lambda \sec \Theta} r dr}{r^2 + z^2} + \int_a^{\sqrt{2}a} \frac{P(\Theta) d^{-\lambda \sec \Theta} r dr}{r^2 + z^2} , \quad (5)$$

where the second integral represents the component due to the portion of the source plane outside a concentric circle of diameter  $2a$ , and  $P(\Theta)$  is the function graphed in Figure 14. The first component of  $D_u$  is readily integrable in terms of tabulated functions and is

$$E_1(\lambda) - E_1 \left[ \frac{\lambda (a^2 + z^2)^{1/2}}{z} \right] . \quad (6)$$

The second integral must be evaluated numerically.

To obtain the total dose rate at the detector positions, we must add a scattered-beam dose component  $D_s$  to the values of  $D_u$  obtained above. This may be accomplished by defining  $D_s(\cos \Theta)$  as the scattered-beam dose component due to source radiation at an angle  $\Theta$  with the centerline of the structure. Then the total dose is

$$D = D_u + D_s , \quad (7)$$

and the scattered-beam dose component is

$$D_s = \int_0^1 D_s(\cos \Theta) d(\cos \Theta) . \quad (8)$$

Values of  $D_s(\cos \Theta)$  are obtained experimentally. We subtract the unscattered component  $e^{-\lambda \sec \Theta}$  from the total measured dose rates of Tables 7 through 12 for centerline positions. The resultant values must be divided by the cosine of the incidence angle, since the intensity of radiation (current per unit area of front plate) was experimentally proportional to  $\cos \Theta$ . The results of this manipulation generate the family of curves given in Figure 15. The integrals under these curves are  $D_s$ , and are recorded in Table 14 for the nine centerline detectors.

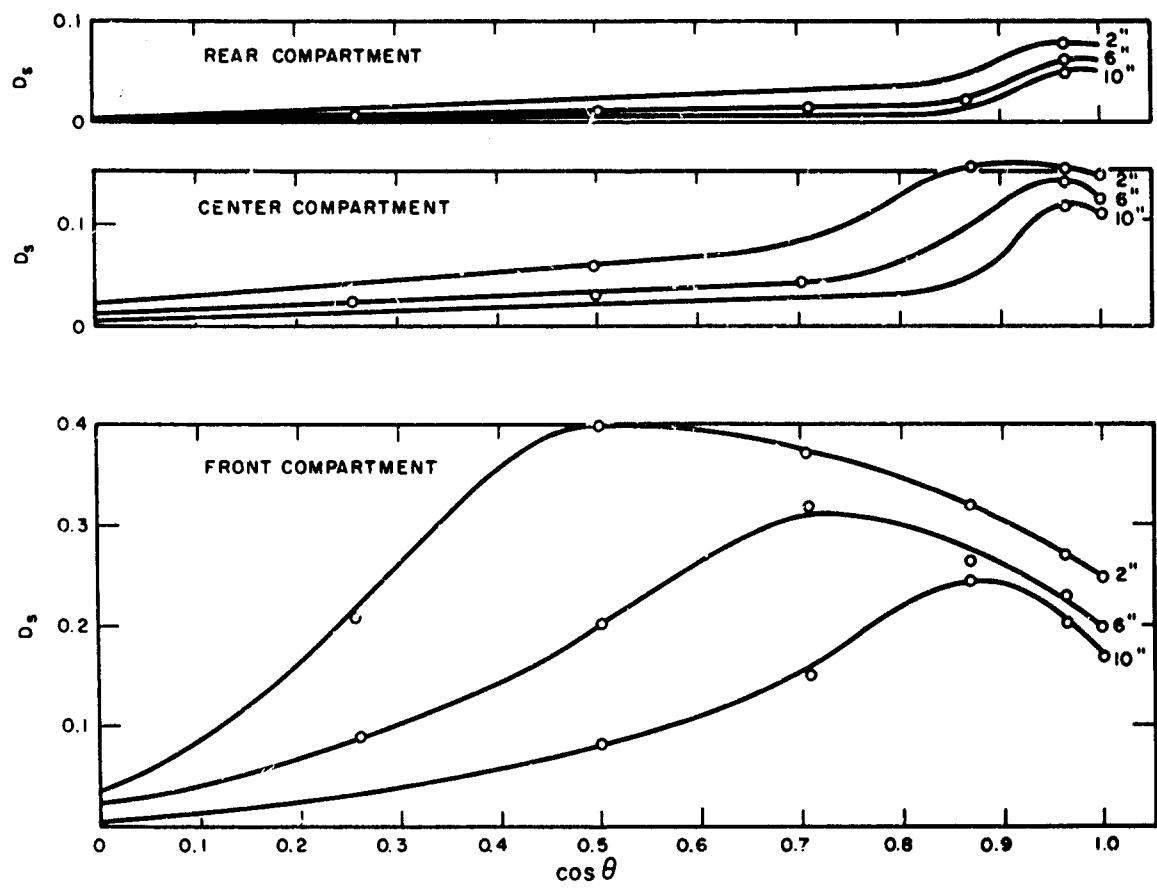


Figure 15. Scattered Component of Dose Rates Along Centerline of Compartments, Due to Incident Radiation and Angles  $\Theta$  with Normal to Front Plate

**TABLE 14**  
**COMPONENTS OF ISOTROPIC ROOF SOURCE DOSE CONTRIBUTION**

Compartment	Detector Plane (in.)	$D_u$	$D_s$	$D(\text{experimental})^*$
Front	2	0.2004	0.2846	0.4850
	6	.1714	.1807	.3521
	10	.1246	.1047	.2293
Center	2	.0276	.0736	.1012
	6	.0204	.0423	.0627
	10	.0196	.0277	.0473
Rear	2	.0040	.0257	.0297
	6	.0034	.0129	.0163
	10	.0028	.0061	.0089

\* Ratio of dose rate with 40 psf floors to dose rate with 0 psf floors.

#### COMPARISON WITH ROOFTOP CONTAMINATION CALCULATIONS

The OCD Engineering Manual<sup>2</sup> presents a method for the calculation of the effects of radioactive contamination on a rooftop. The results obtained in the previous chapter and tabulated above in Table 14 should be comparable to those obtained by this method.

We calculate that a 1 in. steel plate provides an attenuation equivalent to 38.4 psf of water. From this, and from a calculation of the solid angle subtended by the roof at the detector, we obtain the parameters  $X$  (equivalent pounds per square foot) and  $\omega$  (subtended solid-angle fraction). The dose rate due to roof sources is then  $D(\omega, X)$ .



With vanishing  $X$ , the dose rate due to roof sources is readily calculated from an integral. Where the source concentration is such that current from a unit area, in directions about a solid angle  $d\Omega$ , gives a dose rate equal to  $(d\Omega/2\pi)$ , the expression for the dose rate is

$$D = \int_{\text{plane}} \frac{dx dy}{2\pi\rho^2}, \quad (9)$$

where  $\rho$  is the distance from the unit area  $(x, y)$  to the detector. This integral is readily evaluated if the plane is a disk and the detector is located along the disk axis. The dose is then

$$D(\text{without shield}) = -\ln(1 - \omega). \quad (10)$$

To obtain the reduction factor  $R_f$ , one needs to know the ratio of the dose rate due to shielded sources in all directions, to the dose rate due to the same sources when they are unshielded. The shielded dose rate may be decomposed into contributions from sources in various solid angle fractions, so that

$$R_f = \frac{D(\omega_1, X_1) + D(\omega_2, X_2) + \dots}{D_o(2, X_o)}, \quad (11)$$

where  $X_o$  is the shielding provided by 3 ft of air. This ratio is obviously equal to

$$R_f = \left[ \frac{D(\omega_1, X_1)}{D_o(\omega_1, X_o)} \right] \left[ \frac{D_o(\omega_1, X_o)}{D_o(2, X_o)} \right] + \left[ \frac{D(\omega_2, X_2)}{D_o(\omega_2, X_o)} \right] \left[ \frac{D_o(\omega_2, X_o)}{D_o(2, X_o)} \right] + \dots, \quad (12)$$

where  $D_o(\omega_1, X_o)$  may be chosen as the dose rate due to sources in the range of  $\omega_1$ , with negligible shielding  $X_o$  present. Then, the first bracketed ratio in Eq. (12) may be computed by dividing experimental values from Table 14 by values

computed from Eq. (10). The second ratio is equivalent to  $L_c(X_o, \omega_1)$ , as discussed earlier in this chapter under isotropic radiation, with the further observation that  $L(X_o)$  is unity.

Thus, the reduction factor  $R_f$  is the sum of all the dose rate contributions  $C$ . The overhead contribution  $C_o$  is given in the OCD Engineering Manual. In presenting this function, Eisenhower and FitzSimons, the manual authors, utilized Spencer's<sup>7</sup> curves; specifically,  $C_o$  equals the product  $L(X)L_c(X, \omega)$ .

The present experimental data are not exactly applicable to a test of  $C_o$ , since that function was derived for gamma radiation of a spectrum corresponding to early fallout. However, one may compute a similar function from curves of  $L$  and  $L_c$  in Ref. 7, especially for cobalt-60 radiation and a concrete medium. At these gamma energies, the mass attenuation coefficient is remarkably insensitive to the nature of the medium (see, for example, the graph in Ref. 9), and data for concrete may be applied to measurements in steel.

From this line of reasoning, it might be presumed that our data are not too precise a test of the accuracy of the Spencer-Eisenhower-FitzSimons rooftop contamination curves. However, we see in Table 15 that several figures extracted from Table 14 compare well with the dose rates derived from this source. The theory consistently evaluates the dose rate as more than the experiment predicts. Even if we could assign all the error to theory, it would not deviate more than Eisenhower had anticipated, according to Ref. 10.

TABLE 15  
COMPARISON OF EXPERIMENTALLY DERIVED AND  
THEORETICAL ROOFTOP-SOURCE DOSE RATES

X	$\omega$	$R^*$	$D/D_o^\dagger$	$\left(\frac{\text{Theory}}{\text{Exper.}}\right)$
38.4	0.60	0.468	0.352	1.33
76.8	.20	.325	.281	1.15
115.2	.09	.176	.171	1.03

\* Ratios of  $L(X)L_c(X, \omega)/L(o)L_c(o, \omega)$  from Ref. 2, p. 126.

† D from Table 14,  $D_o$  from Eq. (10).

The comparison indicates, however, that a worthwhile effort would be that of measuring the actual rooftop radioactive deposit protection factor  $C_o$  afforded by the roof and overhead floors of a building. The present experiment indicates some departure between the prediction and the measurement, possibly due to separation distance effects or to the separation of the layers (floors) of the shield.

## CHAPTER 5

### COMPARISON WITH MONTE CARLO CALCULATIONS

The analytical methods described in the previous chapter fail to account for the complicated geometry involved in the attenuation of the dose rate at positions such as the center and rear compartments. One method (and perhaps the only comprehensive one in use) of including these complications in the analysis is to employ the so-called Monte Carlo technique.

Essentially, this technique involves the computation of the probability of a photon traversing a particular path (selected at random) and striking the detector. The results of selecting a large number of paths provide an estimate of the transmission probability.

Such a computation has been programmed by Raso and Woolf<sup>8</sup> for machine calculations. The geometry considered is an infinite-plane slab of material that has photons incident on one surface, all with given angles of incidence. The detector, located a distance on the adjacent surface of the slab, counts only photons entering it through a solid angle given by  $\omega$ . As seen in Figure 16, this corresponds closely to counting only photons that originate in a finite plane source subtending the solid angle fraction  $\omega$ .

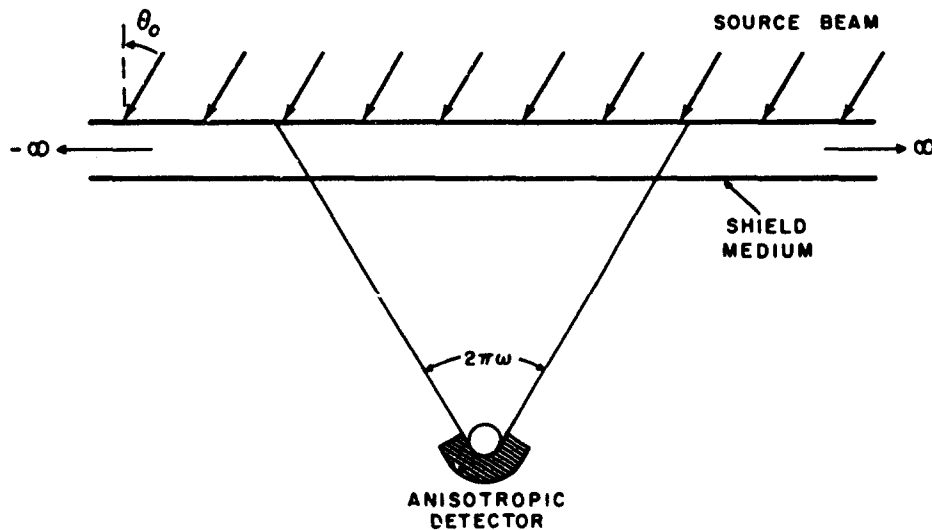


Figure 16. Monte Carlo Program Simulation of Slab Shield Effects

The results of this first computation are directly applicable to measurements in the front compartment of our present egg crate experiment. To obtain center-compartment results, the program determines a source of an incident-angle distribution, determined by the distribution leaving the first shield slab, and applies this to the second slab. In a similar manner, rear compartment results are also possible. (A more detailed explanation of the techniques used can be found in Ref. 8.)

Results obtained by this program are presented as

$$\frac{1}{N} \sum_{i=1}^{M < N} \left( \frac{\mu}{\rho} \right)_i E_i ,$$

where M is the number of photons penetrating to the detector, N the number of photons incident on the slab ("histories"),  $E_i$  the energy of the  $i^{\text{th}}$  photon (in keV), and  $(\mu/\rho)_i$  the mass absorption coefficient of air for the  $i^{\text{th}}$  photon. Now, if we divide this expression by  $(\mu/\rho)_0 E_0$ , where the subscript refers to the source energy, the results are transformed to the ratio of detected energy to incident energy. This is essentially the dose ratio, and comparison may be made with experimental results.

It should be mentioned here that the actual program used includes the photoelectric effect and pair production as absorption processes only, thereby neglecting the dose contribution due to pair annihilation, bremsstrahlung, and X-ray fluorescence. However, these processes contribute very little to the dose rate, inasmuch as the pair and photoeffect cross sections represent only 2% of the total iron cross section at 1.25 MeV, and inasmuch as these softer radiations are more easily attenuated by the medium.

## RESULTS OF NORMAL INCIDENCE COMPUTATIONS

The results of this calculation for the centerline of the front compartment are plotted in Figure 17, along with the three centerline measurements for each shield

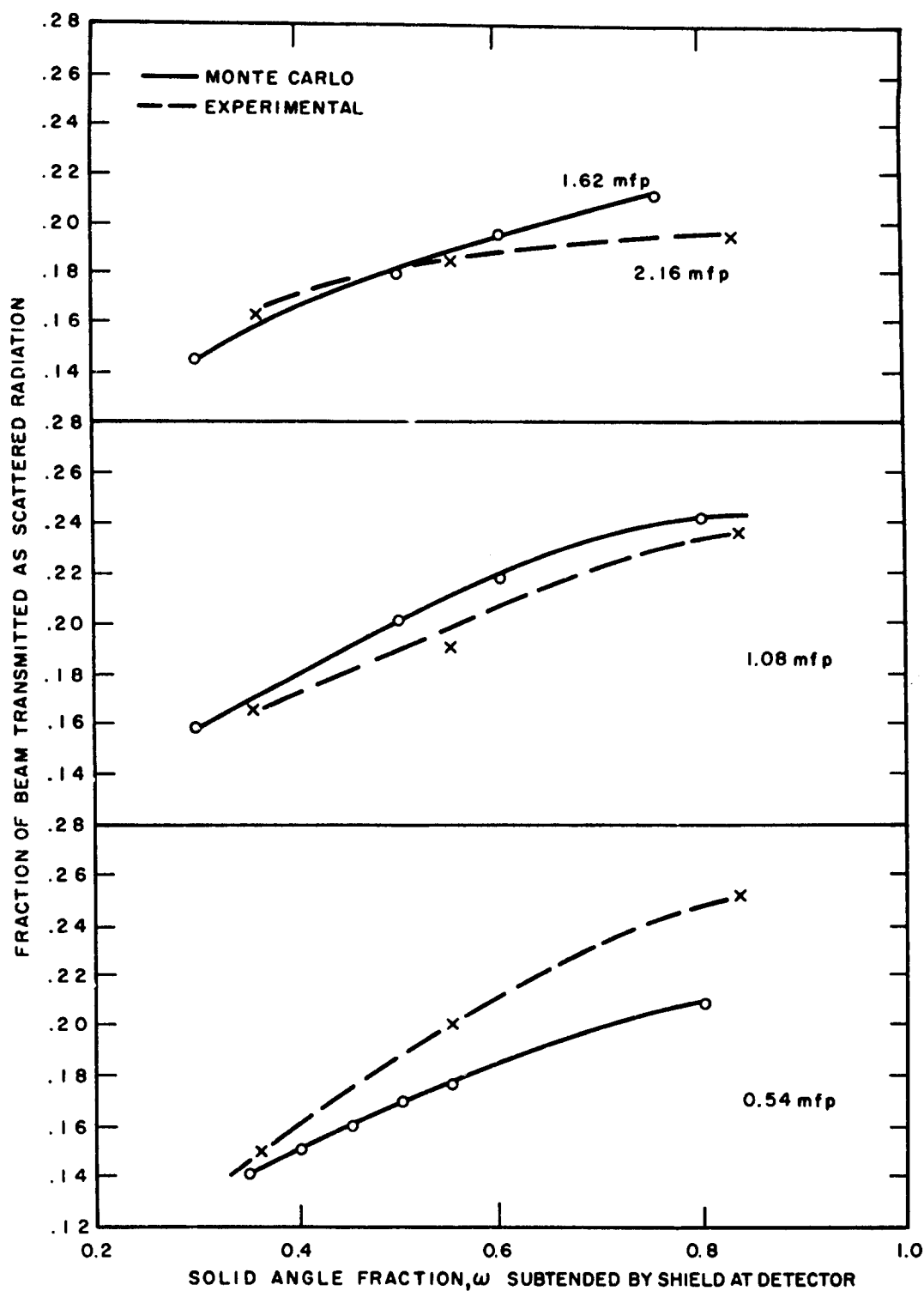


Figure 17. Comparison of Monte Carlo Prediction of Scattered Dose Rates with Centerline Measurements (Front compartment)

thickness. Normally incident radiation is considered. In analyzing this figure, it should be noticed that the origin is not included in the graph, so that differences between Monte Carlo and experimental results are magnified.

The 20 psf structure case was the subject of a further Monte Carlo calculation. The current angular distribution, as well as the intensity, was calculated at the face of the second plate, and this result was used as a source to calculate dose rate distributions in the center compartment. In addition, the current at the face of the third plate was calculated, providing source for calculation of the radiation in the rear compartment. At centerline detectors, only those dose rates due to scattered radiation were obtained. These were presented in keV absorbed per gram of detector, per second, and are therefore comparable to values presented in Table 2 through the formula

$$D_s = 33.25 \left( \frac{D}{D_0} - e^{-\lambda} \right), \quad (1)$$

where  $D_s$  is the scattered photon dose rate in keV/g/sec,  $D/D_0$  is a dose ratio tabulated in Table 2, and  $e^{-\lambda}$  is the uncollided-photon portion of the dose rate. The factor 33.25 equals  $10^3 (\mu_a/\rho)E_0$  and is introduced as described above. By subtracting the uncollided beam portion, a more sensitive comparison of the structure's geometry-dependent portion of the dose rate is possible.

The Monte Carlo results are compared with experimental results in Table 16. The results for the center and rear compartments neglect the presence of side walls and walls to the rear of the detector. The magnitude of these contributions may be seen from the double entries for the front compartment. Here, walls to the rear of the detector have been neglected for the first entry; they are included together with side walls for the second entry. The experimental values (with no side walls) are still higher than either of the Monte Carlo values. In fact, this comparison is the poorest of the three compartments, and was the same comparison that was so poor in Figure 17.

**TABLE 16**  
**COMPARISON OF MONTE CARLO AND EXPERIMENTALLY DERIVED**  
**DOSE RATES FOR NORMALLY INCIDENT BEAM ON 20 PSF WALLS**  
 (See Table 2)

Compartment	Detector Plane (in.)	Experimental	Monte Carlo	Monte Carlo, plus Walls and Floors
Front	2	8.45	6.88	7.22
	6	6.78	6.09	6.69
	10	5.12	4.84	5.87
Center	2	8.21	7.80	—
	6	6.90	6.87	—
	10	5.22	5.69	—
Rear	2	6.95	6.81	—
	6	5.61	6.13	—
	10	4.62	5.19	—

The value of the uncollided portion of the dose rate in the front compartment (with 20 psf walls) is 0.58. Thus, an experimental measurement of 0.84 in the center of the compartment is fully 70% due to uncollided photons. A slight error in the measurement results in a large error in the calculation of the scattered portion in such a situation. We believe this to be the case in the thin-walled front compartment, and thus prefer the Monte Carlo result for the reason explained below.

Consider a buildup factor of the form  $(1 + \lambda)$  for a beam of radiation, where  $\lambda$  is the mean free paths of shield material. That is,

$$D = D_0 (1 + \lambda) e^{-\lambda} , \quad (2)$$



where  $D/D_0$  is the ratio of the dose rate with shield in place to the dose rate without shield in place. This form of buildup factor is one of those commonly accepted.<sup>11</sup> Since the uncollided photon contribution to the dose rate is given by  $D_0 e^{-\lambda}$ , the scattered photon contribution  $D_s$  is given by

$$D_s = D_0 \lambda e^{-\lambda} . \quad (3)$$

The value of  $\lambda$  that provides the maximum value of  $D_s$  occurs when the differential of this expression with respect to  $\lambda$  vanishes. Thus,

$$e^{-\lambda} (1 - \lambda) = 0 \quad (4a)$$

$$\lambda = 1 . \quad (4b)$$

In other words, the scattered-photon dose rate reaches its maximum 1 mfp into the material, provided that the buildup factor is reasonably approximated by  $(1 + \lambda)$ . Since the Monte Carlo results in Table 16 show this trend, they would seem more reliable than the experimental measurements.

In the other compartments, the results are more compatible. Agreement is within 10%, and in most cases within 5%. Here, it is difficult to assign these small deviations to underlying difficulties with either method, and perhaps it would be a useless task to attempt to do so.

## RESULTS OF SLANT INCIDENCE COMPUTATIONS

The results of the angular runs (Tables 8 through 12) were compared with Monte Carlo calculations for the centerline detectors of the front compartment. These comparisons are presented in Table 17. The Monte Carlo code presumed a constant intensity, but since we reduced the intensity of radiation incident on the front plate by tilting the experimental structure, the appropriate form of Eq. (1) for these comparisons of a 40 psf structure is

$$D_s(\Theta) = \frac{33.25}{\cos \Theta} \left( \frac{D(\Theta)}{D_0} - e^{-\lambda/\cos \Theta} \right) . \quad (5)$$

TABLE 17  
COMPARISON OF MONTE CARLO AND EXPERIMENTALLY DERIVED  
DOSE RATES FOR SLANT RADIATION ON 40 PSF STRUCTURE

cos $\theta$	Detector Plane (in.)		
	2	6	10
Monte Carlo			
1.0	7.91	6.94	5.72
0.75	8.38	6.68	4.71
0.50	8.47	6.03	3.66
0.25	6.25	4.15	2.36
0.00	2.08	1.59	0.99
Experimental			
1.0	8.99	7.33	6.00
0.96593	8.72	7.34	6.65
0.86603	9.32	7.40	7.01
0.7071	9.55	7.66	2.02
0.5000	9.62	5.97	2.52

In general, it may be seen that agreement is quite good. The 40 psf walls correspond to approximately 1 mfp, which reduces the experimental difficulty discussed earlier in this chapter under normal incidence computations, and does not provide too great a difficulty for the code in calculating histories.

#### ISOTROPICALLY INCIDENT RADIATION

Combining the results of several Monte Carlo calculations for centerline dose rates due to radiation incident at various angles gives a reasonable estimate of the total dose rate due to isotropic radiation. (A similar effort was described in Chapter 4, for the experimental results.) Only the scattered photon component was

considered in the computations, since the direct component may be easily computed analytically, as was done above.

So far in this chapter we have considered only parallel solutions for a particular problem by using both Monte Carlo computations and experimental measurements. Monte Carlo computations were performed for isotropically incident radiation for structures of 20 psf and 40 psf walls. It is felt that the previous sections justify a measure of reliance in the agreement of results of the two methods. Therefore, the two calculations for structures of differing wall thicknesses should present a limited range of evaluations of the isotropic radiation problem. However, because of the ease of solution, the isotropic radiation response was computed for 40 psf walls for the front compartment.

Figures 18 through 21 present the constructed isotropic-source reduction factor versus the solid-angle fraction  $\omega$  for the various wall thicknesses and compartments of the structure. The Monte Carlo and experimental points are compared in each figure with the corresponding transport solution of Ref. 7. This affords a two-way comparison of data with the basic curves for the roof source reduction factor of the OCD Engineering Manual.<sup>2</sup> To compare these data with Spencer's transport solution, it is necessary to subtract from his solution  $L(X)L_c(X, \omega)$ --the component due to uncollided radiation. This leads to the equation

$$D_s = BE_1(\lambda_0)L(X)L_c(X, \omega) - \left[ E_1(\lambda) - E_1(\lambda/1 - \omega) \right]. \quad (6)$$

Here,  $\lambda$  is the shield thickness in mean free paths, and is therefore proportional to  $X$ . The exponential function  $E_1(\lambda)$  enters the expression as it did in the previous section. The first term on the right in Eq. (6) represents the total dose rate, and the second represents the unscattered photon contribution. The dose rate in air 3 ft from an infinite plane of this source is given by the expression  $BE_1(\lambda_0)$ , where  $\lambda_0$  is the shield thickness of the air under standard conditions. The function  $D_s$  defined by Eq. (6) is plotted as the transport solution in Figures 18 through 21. We obtain the buildup factor  $B$  from a note by Berger and Spencer.<sup>12</sup> Thus, except for the exponential integrals, the expression for  $D_s$  is derived from transport calculations.

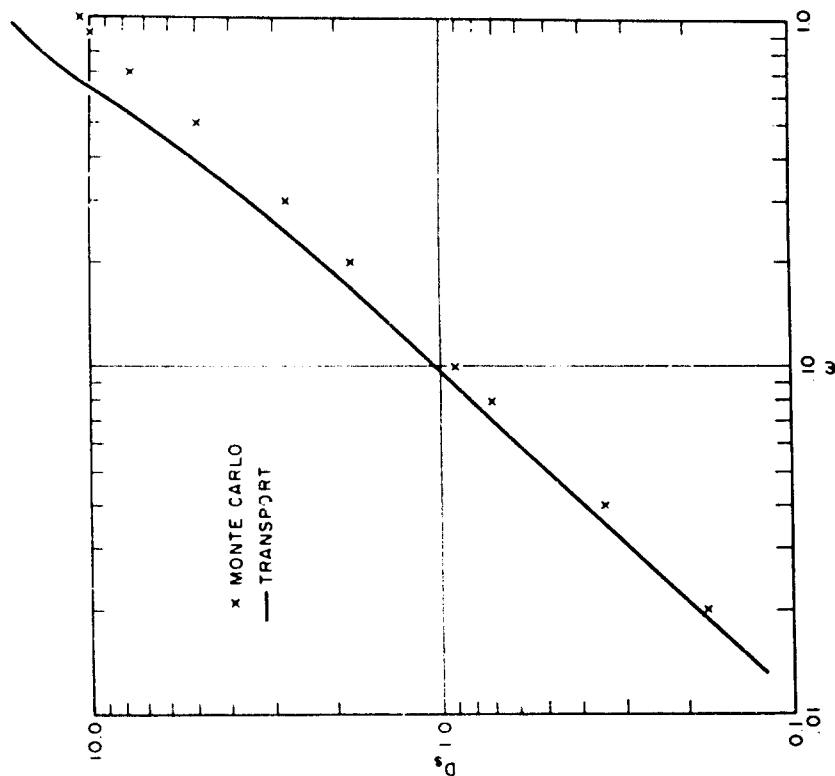


Figure 18. Comparison of Scattered Component of Flux Due to Rooftop Radiation as Determined by Three Methods; Detector in Front Compartment of 40 psf Structure

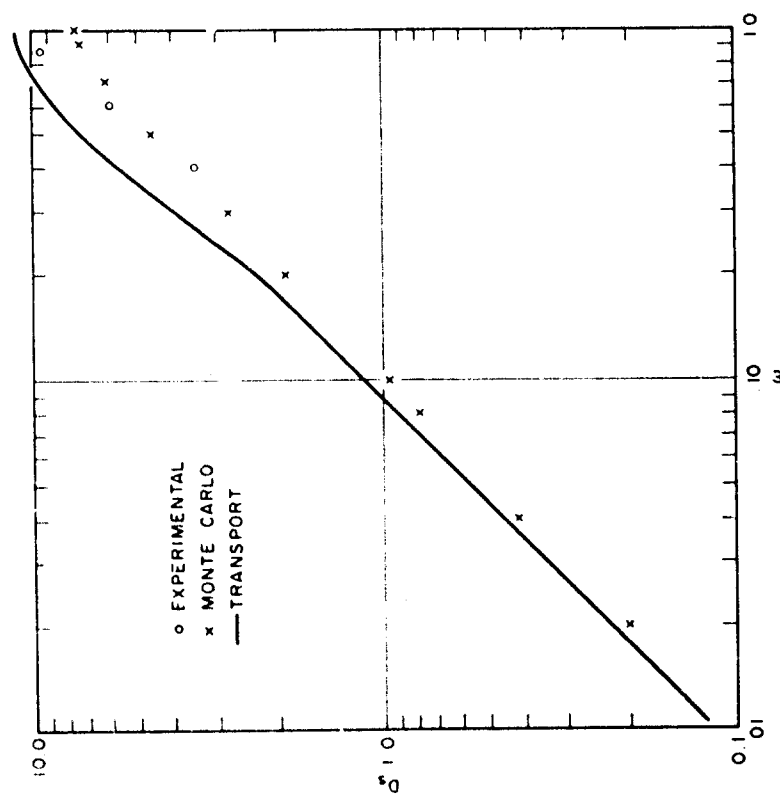


Figure 19. Monte Carlo and Transport Solutions for Scattered Flux; Detector on Centerline of Front Compartment of 20 psf Structure

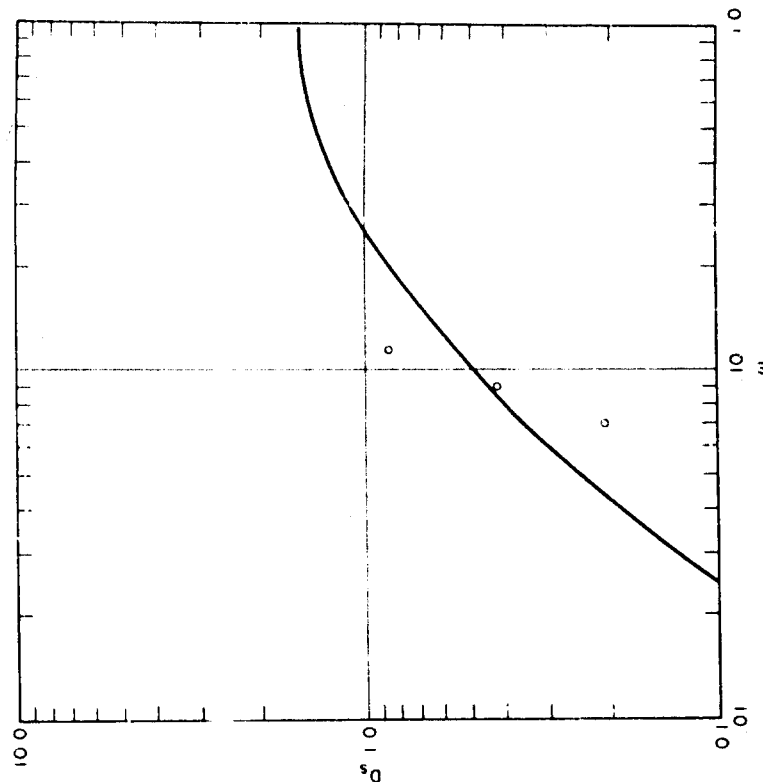


Figure 21. Experimental Points and Transport Curve for Scattered Flux; Detector on Center-line of Rear Compartment of 40 psf Structure

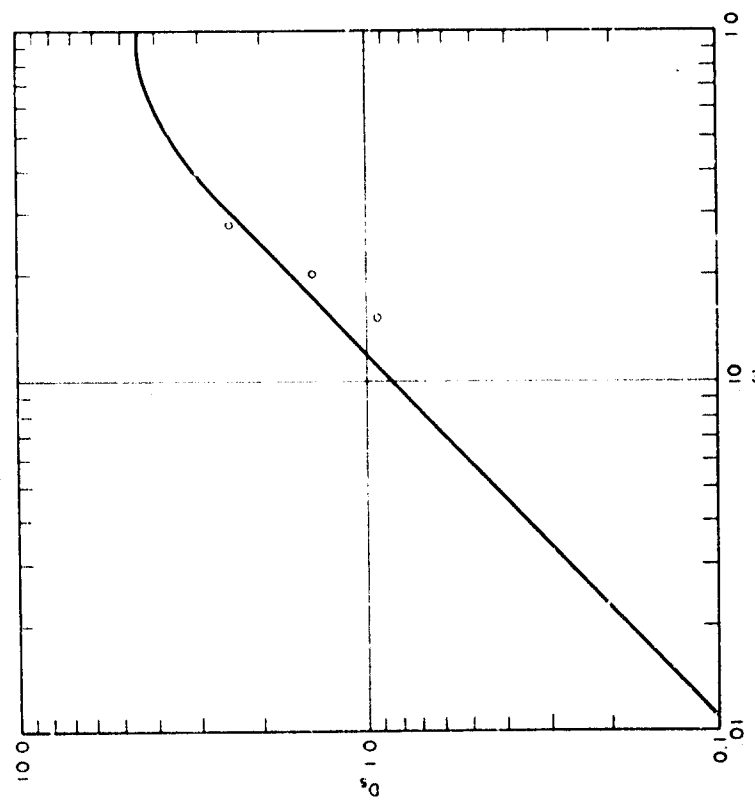


Figure 20. Experimental Points and Transport Curve for Scattered Flux; Detector on Center-line of Center Compartment of 40 psf Structure

## CHAPTER 6

### CONCLUSIONS AND RECOMMENDATIONS

#### CONCLUSIONS

##### SHIELDING

Several general conclusions may be drawn regarding the gamma shielding offered by a compartmented structure.

1. It appears evident that backscatter represents a small contribution to the dose rate. This was on the order of 2% in the experiment, although in a situation where a structure composed of a lower atomic number material is exposed to somewhat lower energy quanta of radiation, the contribution would be expected to be somewhat higher.
2. The experimental results indicate that dose rates are dependent not only on the shield thickness in front of a given detector, but also on the distribution of the shield. Detectors in each compartment, behind the same mass thickness, show a marked drop in dose rate as the distance from the shield slab increases. Further, the experimental data (Tables 2 through 4) show one shield slab is generally less effective than two slabs, each half as thick.

##### METHODS OF SOLUTION

The figures and tables in this report show that there is good agreement among the three methods of solution—experimental, Monte Carlo, and moments solution of transport theory. Thus, any problem of gamma shielding by thin shields should be solvable by any of the three methods, given sufficient time and care, for there are no surprises in the physics involved. However, differences arise when one considers the effort required.

1. The transport solution probably takes the most effort, but gives answers that are more self-consistent, if not truer. Difficulties are encountered only when the context of the problem is changed; for example, we did not have such a solution to compare with the

effect of looking at a finite cross section of a shielded mono-directional source. Such a case would require an extension of the graph collection of the moments method solutions.

2. The Monte Carlo program appears to be excellent for its intended purpose—the solution of a compartmented structure shielding effect. Again, however, the method requires time and patience and, therefore, far from all of the experimentally measured points were checked by the computer calculations.
3. In the ultimate analysis, the experimental approach is the best, even though the experiment here is far from ideal. It is difficult to assess the effects of humidity, background, and mechanical shock on each dosimeter's residual charge. The Styrofoam holders present a small, variable shielding effect. Finally, small systematic errors in the measurement of a total exposure can lead to gross errors in the calculated exposure to scattered photons, particularly when the unscattered component is much greater than the scattered. As a result, the internal consistency of the experimental results is considerably lower than in the other cases. Nevertheless, the versatility of the experimental approach, its independence of the mathematical model that must be otherwise developed, and its economical aspects make it a formidable tool for cross-checking a previous solution as well as researching an unknown one.

### RECOMMENDATIONS

1. The Monte Carlo code for attenuation of radiation in a compartmented structure appears to be of an accuracy to warrant its further use in similar shielding studies of compartmented structures.

2. This study indicates that the OCD Engineering Manual overestimates the dose rate obtained behind multiple thin layers. An experiment with isotropic sources on the face of the shield, with a variable number of interposing layers, should be performed to further explore this discrepancy. An analysis should be made to see if the rooftop-source reduction factor  $C_0$ , defined in the Engineering Manual, need be modified to account for interior floor spacing in a multistoried building. (Block-house experiments<sup>13</sup> have indicated that the theoretical reduction factor provides quite a conservative estimate of the experimental factor when floors exist between roof and detector.)

#### REFERENCES

1. Office of Civil Defense, "Guide for Architects and Engineers," NP-10-2 (May, 1960).
2. Office of Civil Defense, "The Design and Review of Structures for Protection from Fallout Gamma Radiation," rev. ed. (1 October 1961).
3. J. F. Batter, A. W. Starbird, and Nancy-Ruth York, "Final Report on the Effect of Limited Strips of Contamination on the Dose Rate in a Multistory, Windowless Building," Technical Operations Research, Report No. TO-B 62-58 (August, 1960).
4. F. W. Sanders, J. A. Auxier, and J. S. Cheka, "A Simple Method of Minimizing the Energy Dependence of Pocket Ionization Chambers," Health Physics 2, 308-309 (1960).
5. Technical Operations, Incorporated, "Instruction Manual for Tech/Ops Model 556 Dosimeter Charger-Reader" (March, 1964).
6. M. J. Berger, "Calculation of Energy Dissipation by Gamma Radiation Near the Interface Between Two Media," J. Appl. Phys. 28, 1502 (1957).



7. L. V. Spencer, "Structure Shielding Against Fallout Radiation from Nuclear Weapons," National Bureau of Standards, Monograph 42 (1 June 1962).
8. D. J. Raso and S. Woolf, "Final Report on the Dose Resulting from 1.25 MeV Plane Source Behind Various Arrangements of Iron Barriers," Technical Operations Research, Report No. TO-B 64-49 (August, 1964).
9. P. F. Berry, "Gamma-Ray Attenuation Coefficients," *Nucleonics* 19(6), 62 (June, 1961).
10. C. Eisenhauer, "An Engineering Method for Calculating Protection Afforded by Structures Against Fallout Radiation," National Bureau of Standards, Report No. 7810 (28 February 1963).
11. "Radiation Shielding," in Reactor Handbook, 2nd edition, ed. E. P. Blizard (New York, N. Y.: John Wiley & Sons, Inc., 1962) IIIB, 141.
12. Martin J. Berger and Lewis V. Spencer, "Penetration of Gamma Rays from Isotropic Sources through Aluminum and Concrete," National Bureau of Standards, Technical Note 11 (11 May 1959).
13. Kansas State University, Department of Nuclear Engineering, "Final Report of OCD Summer Institute on Fundamental Radiation Shielding Problems as Applied to Nuclear Defense Planning" (October, 1963).